European Journal of Mechanics / B Fluids 105 (2024) 119–137

Contents lists available at ScienceDirect

European Journal of Mechanics / B Fluids

journal homepage: www.elsevier.com/locate/ejmflu

Direct numerical simulation of laminar, transitional and turbulent radially inward flow between closely spaced corotating disks

S. Klingl [a,*], S. Lecheler [a], M. Pfitzner [b]

[a] Department of Technical Thermodynamics, Faculty of Mechanical Engineering, Universität der Bundeswehr München, Germany
[b] Institute of Thermodynamics, Faculty of Aviation and Aerospace Engineering, Universität der Bundeswehr München, Germany

ARTICLE INFO

Keywords:
Direct numerical simulation
Linear stability analysis
Tesla turbine
Friction turbine
Rotating disk flow
Nek5000

ABSTRACT

This study describes direct numerical simulation (DNS) of radially inward spiralling corotating disk flow with a narrow disk spacing, using the open source solver Nek5000 and the supercomputer SuperMUC-NG at Leibniz Supercomputing Centre. Knowledge about laminar and turbulent regime boundaries in this flow scenario is important for modelling and performance prediction of friction turbines. Simulations are performed in differently sized sections of the flat annulus that is formed by two opposing corotating disk surfaces. Three sets of operating conditions are covered, from the laminar, transitional and turbulent region of a previously determined stability chart respectively. Directly downstream of the inlet boundary, the flow is artificially perturbed with a random body force acting normal to the disk surfaces. Fourier analysis of the DNS flow field reveals that the artificial perturbation is dampened across all wavenumbers for the laminar conditions, while at the transitional conditions a small range of modes is weakly amplified towards the outlet. The identified unstable modes were previously correctly predicted by linear stability analysis. Comparison to experimental velocity profile measurements from a previous study at the same transitional operating conditions suggests strongly perturbed flow during the experiment. For inflow conditions leading to turbulent flow, average velocity profiles from DNS coincide with those from experiment and from commercial fluid simulation software with turbulence modelling (ANSYS CFX). Close to the walls, turbulent dissipation and turbulent kinetic energy distributions do not agree with the ANSYS CFX results. Friction Reynolds number settles at about 118 after turbulent flow has developed from the initial perturbation. Two point correlations and corresponding energy spectra are presented.

1. Previous work and goals

Radially inward flow between corotating disks is found in friction turbines, where the rotor consists of a set of circular disks that is driven by a working medium flowing in between them along an inward spiral path. Fig. 1 visualizes the basic setup. Performance prediction of such turbines can be done efficiently through analytical and numerical flow models of the inter-disk flow based on simplified Navier–Stokes equations. Various approaches exist for laminar flow, such as the asymptotic solution by Breiter and Pohlhausen [1], the method based on parabolic velocity profiles by Beans [2] or the series-based approach by Batista [3]. For modelling turbulent flow, apart from conventional fluid simulation with turbulence modelling, an approach based on power law velocity profiles has been suggested by Beans [2]. The selection of a suitable modelling approach requires beforehand knowledge about the flow regime. Regime boundaries were previously determined through linear stability analysis by Flaherty and DiPrima [4] and Klingl et al. [5], and through experiment by Pater et al. [6] and Dibelius and Nendl [7]. The new results from direct numerical simulation (DNS) that are presented here are intended to give further insight into the nature of flow instability inside the corotating cavity and validate previous results from theory and experiment.

An important classical example of flows involving rotating disks is the flow in a semi-infinite medium above a single rotating disk, known as von Kármán flow. It can be characterized by a single Reynolds number that is calculated from disk rotational speed, radial position and fluid viscosity. Laminar-turbulent transition mechanics in von Kármán flow are well researched. As an example, the recent study by Appelquist et al. [8] breaks down the transition mechanism involving secondary, absolute and global instability phenomena. Rotating disk flow with imposed free stream radial velocity is analysed by Turkyilmazoglu [9], who finds an overall stabilizing effect of radial outward free stream velocity on the flow.

* Corresponding author.
E-mail address: stefan.klingl@unibw.de (S. Klingl).

https://doi.org/10.1016/j.euromechflu.2024.01.007
Received 4 September 2023; Received in revised form 20 December 2023; Accepted 11 January 2024
Available online 15 January 2024

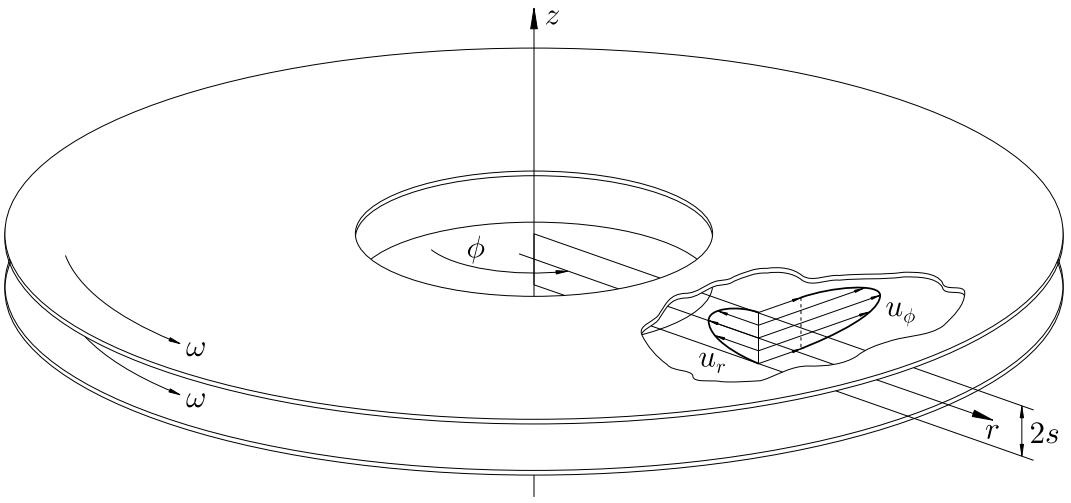

Fig. 1. Schematic view of the flow setup.

Flows involving two rotating disks bear additional complexity, since radial flow rate, disk rotational speed, disk spacing and inlet flow direction can be chosen independently of each other. Fundamentally different types of flows develop between the disks, depending on the choice of characteristic parameters. This study investigates a set of operating conditions that resembles the friction turbine application, with narrow disk spacing and spiralling radial inward flow that induces a torque on the disk surfaces in the direction of rotation. The simulations share some similarities with the direct numerical simulation of von Kármán flow by Appelquist et al. [10], which also uses Nek5000 and similarly implemented body forces for perturbing and dampening the flow.

One of the goals of the present study is to numerically reproduce some of the conditions which were analysed before experimentally by Schosser [11]. The author obtained spatially resolved, temporally averaged velocity distributions from inside the disk gap through 3D particle tracking velocimetry (PTV) measurements using a specialized test facility featuring a single corotating disk gap with optical access and air as working medium. Comparing the experimental velocity profiles to results from DNS and linear stability theory allows understanding the flow conditions that were prevalent in the experiment.

Another main objective of the present study is to verify results from linear stability analysis. Klingl et al. [5,12] describe three different approaches to identify unstable modes that are amplified by the flow and possibly lead to transition into turbulence. A stability limit can be located below which all flow disturbances are dampened, as a function of a mass flow parameter and a rotational speed parameter. Contrary to von Kármán flow, no absolute instability is found for the narrow disk spacing analysed in Klingl et al. [5]. As a consequence, disturbances are expected to only propagate downstream and the flow inside the domain will always return to an undisturbed state, unless a disturbance is applied continuously in time.

There are further theoretical and experimental studies regarding flow stability that can be applied to Tesla turbine flow, for example by Pater [13], Pater et al. [6], Wollkind and DiPrima [14] and Flaherty and DiPrima [4]. A brief overview and comparison is provided by Klingl et al. [12]. The results roughly agree, instability in the experiments is however observed at, or even slightly below, the theoretical stability limit. This has yet to be explained.

Finally, direct numerical simulation results give the opportunity to compare turbulence parameters and average velocity profiles to simulation data obtained from conventional fluid simulation with turbulence modelling. The comparison gives an impression of how accurately the conventional methods are predicting the flow field in the turbulent and transitional regime.

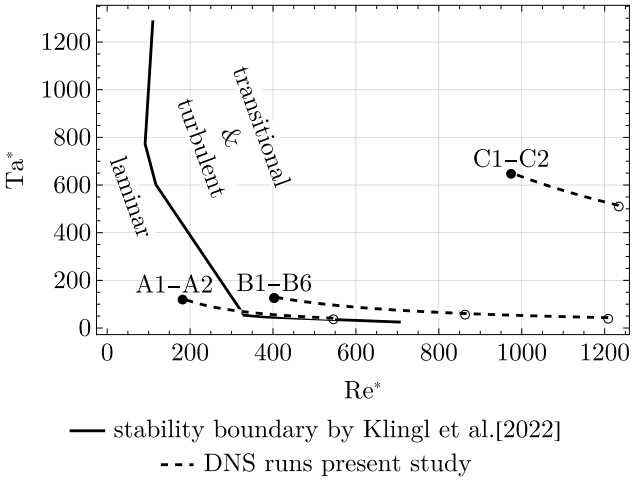

Fig. 2. Location of the computations in the stability plane. The stability boundary from linear theory is shown as solid line, the dashed lines indicate the ranges of local parameters covered by the computations, with filled circles referring to the inlet radius r_1 and empty circles to the outlet radius r_2.

The main investigations are performed for laminar, transitional and turbulent operating conditions, labelled with A, B and C respectively. Fig. 2 locates the computations relative to the theoretical stability boundary by Klingl et al. [5]. The local Reynolds number Re^* can be interpreted as radial mass flow parameter, the local Taylor number Ta^* as rotational speed parameter. Definitions are given in the next section. The solid points refer to the inlet radius r_1, where local and global parameters are equal, so $\mathrm{Re}^*(r_1) = \mathrm{Re}$ and $\mathrm{Ta}^*(r_1) = \mathrm{Ta}$.

The study is conducted using the open source fluid simulation code Nek5000 [15]. Some key results of the direct numerical simulation are also shown in a dissertation that is expected to be published towards the beginning of 2024, refer to Klingl [16]. Explanations of symbols and abbreviations are given in Appendices A and B.

2. Study outline

2.1. Definitions

The numerical method solves the incompressible Navier–Stokes equations in a stationary frame of reference.

$$\left(\frac{\partial \boldsymbol{U}}{\partial T} + (\boldsymbol{U}\cdot\nabla)\boldsymbol{U}\right) = \boldsymbol{F} - \nabla P + \frac{\mathrm{Re}}{\sigma}\Delta\boldsymbol{U} \tag{1}$$

$$\nabla \cdot \boldsymbol{U} = 0 \tag{2}$$

$\boldsymbol{F}$ is an artificial body force vector for perturbing the flow in the inlet region and dampening in the outlet region. A cylindrical coordinate system is employed, using the coordinates R, ϕ and Z and the velocity vector $\boldsymbol{U} = (U_r, U_\phi, U_z)$. Throughout this study, the circumferential velocity components u_ϕ and U_ϕ are to be understood as absolute velocities, relative to a stationary frame of reference.

Simulations are performed in terms of nondimensional parameters, with the disk outer radius r_1 as a reference length and the average radial fluid velocity at the disk outer radius $\hat{u}_{r1}$ as a reference velocity. Consequently, dimensionless quantities are expressed as follows:

$$R = \frac{r}{r_1}, \quad Z = \frac{z}{r_1} \tag{3}$$

$$U_r = \frac{u_r}{\hat{u}_{r1}}, \quad U_\phi = \frac{u_\phi}{\hat{u}_{r1}}, \quad U_z = \frac{u_z}{\hat{u}_{r1}} \tag{4}$$

$$P = \frac{p}{\rho \hat{u}_{r1}^2}, \quad T = \frac{t\,\hat{u}_{r1}}{r_1} \tag{5}$$

The velocity $\hat{u}_{r1}$ is the absolute value of the integral average velocity at the radial position r_1. The hat indicates averaging in z. The same way, an average circumferential inlet velocity component $\hat{u}_{\phi 1}$ can be computed.

$$\hat{u}_{r1} = \hat{u}_r(r_1) = \left| \frac{1}{2s} \int_{-s}^{s} u_r(r_1, z) \mathrm{d}z \right| \tag{6}$$

$$\hat{u}_{\phi 1} = \hat{u}_\phi(r_1) = \left| \frac{1}{2s} \int_{-s}^{s} u_\phi(r_1, z) \mathrm{d}z \right|. \tag{7}$$

The averages are independent of time and circumferential position because the boundary conditions at r_1 are stationary and axisymmetric. They are related to each other through the inlet flow angle α_1:

$$\alpha_1 = \arctan\left(\frac{\hat{u}_{r1}}{\hat{u}_{\phi 1}} \right) \tag{8}$$

Axisymmetric radial and circumferential inlet velocity distributions are given as boundary condition at the outer disk radius r_1 and an outlet condition at the inner radius r_2. At the surfaces in axial direction, a wall velocity corresponding to rotation around the centre of the disks is imposed. The circumferential boundaries are periodic.

The nondimensional parameters that govern the flow are:

$$\mathrm{Re} = \frac{s\hat{u}_{r1}}{\nu} = \frac{\dot{m}}{4\pi r_1 \mu} \tag{9}$$

$$\mathrm{Ta} = \frac{s r_1 \omega}{\nu} \tag{10}$$

$$\sigma = \frac{s}{r_1} \tag{11}$$

The Reynolds number is based on radial mass flow, Taylor number is based on wall rotational speed. The reference length for Reynolds and Taylor number is half the disk spacing s. Since the reference length in the present setup is the outer disk radius, the aspect ratio σ in introduced in addition. The domain boundaries in radial and axial direction are located in nondimensional parameter space at:

$$R_{min} = R_2 = \frac{r_2}{r_1} \tag{12}$$

$$R_{max} = R_1 = 1, \tag{13}$$

$$Z_{min} = -\sigma \tag{14}$$

$$Z_{max} = \sigma \tag{15}$$

For comparison of results in different domains, it is useful to drop the somewhat arbitrary reference length r_1 and express parameters as function of the local radial position r.

$$\mathrm{Re}^*(r) = \frac{s\hat{u}_r(r)}{\nu} = \frac{\dot{m}}{4\pi r \mu} \tag{16}$$

$$\mathrm{Ta}^*(r) = \frac{s r \omega}{\nu} \tag{17}$$

$$\sigma^*(r) = \frac{s}{r} \tag{18}$$

Each computation thus covers a range of local nondimensional parameters, limited by the set of values corresponding to r_1 and r_2.

$$\mathrm{Re} = \mathrm{Re}^*(r_1) < \mathrm{Re}^*(r) < \mathrm{Re}^*(r_2) \tag{19}$$

$$\mathrm{Ta}^*(r_2) < \mathrm{Ta}^*(r) < \mathrm{Ta}^*(r_1) = \mathrm{Ta} \tag{20}$$

$$\sigma = \sigma^*(r_1) < \sigma^*(r) \quad < \sigma^*(r_2) \tag{21}$$

The parameter ranges covered by the direct numerical simulations, were previously shown in Fig. 2.

For analysing turbulent flow, the wall friction based velocity scale, length scale and Reynolds number are defined as:

$$u_\tau = \sqrt{\frac{\tau_w}{\rho}} \tag{22}$$

$$\delta_v = \frac{\nu}{u_\tau} \tag{23}$$

$$\mathrm{Re}_\tau = \frac{u_\tau s}{\nu} \tag{24}$$

$$z^+ = \frac{z}{\delta_v} \tag{25}$$

In dimensionless parameter space, these are:

$$U_\tau = \sqrt{\mathcal{T}_w} \tag{26}$$

$$\Delta_v = \frac{\sigma}{\mathrm{Re} U_\tau} \tag{27}$$

$$\mathrm{Re}_\tau = \mathrm{Re} U_\tau \tag{28}$$

$$Z^+ = \frac{Z}{\Delta_v} \tag{29}$$

To account for radial inhomogeneity of the flow, the domain is divided into radial sectors, in each of which the average nondimensional wall shear stress $\mathcal{T}_w$ is computed from multiplying the viscous stress tensor with a corresponding surface normal at each wall mesh point and summing over all wall mesh points in the sector. Consequently, all friction parameters are also dependent on the radial position R.

For further analysis of turbulent flow fields, one-dimensional two point correlations are introduced.

$$R_{ij}(\boldsymbol{X}_0, X_k) = \overline{U_i'(\boldsymbol{X}_0) U_j'(\boldsymbol{X}_0 + X_k)} \tag{30}$$

where i, j and k can each be either coordinate direction r, ϕ or z. The local coordinate X_k originates at the point $\boldsymbol{X}_0$ and runs along a line in coordinate direction k from X_{kmin} to X_{kmax}. The overbar denotes temporal averaging. U_i' is the fluctuating component of the nondimensional velocity as in $U_i = U_i' + \bar{U}_i$. As an example, $R_{rr}(\boldsymbol{X}_0, X_\phi)$ correlates the radial velocity component at $\boldsymbol{X}_0$ with its own value at some distance X_ϕ in circumferential direction. Numerical data for R_{ij} is available on the simulation mesh. Energy spectra result from interpolation of R_{ij} onto an evenly spaced mesh and taking the discrete Fourier transform.

$$E_{ij}(\boldsymbol{X}_0, \kappa_{kc}) = \frac{2}{m} \sum_{b=0}^{m-1} R_{ij}(\boldsymbol{X}_0, X_{kb}) \exp(-2\pi \mathrm{i}\ c\ b/m) \tag{31}$$

$$c = 0, 1, \ldots, m-1. \tag{32}$$

The κ_{kc} are wavenumbers in coordinate direction k, X_{kb} are the discrete values of the coordinate X_k at mesh point index b and m is the number of mesh points along the correlation line. The factor of two follows the convention by Pope [17]. The series indices b and c relate to the discrete wavenumbers and coordinates the following way:

$$\kappa_{kc} = \frac{2\pi\ c}{X_{kmax} - X_{kmin}} \tag{33}$$

$$X_{kb} = X_{kmin} + (X_{kmax} - X_{kmin}) \frac{b}{m} \tag{34}$$

$R_{ij}(\boldsymbol{X}_0, X_{kb})$ can be retrieved by:

$$R_{ij}(\boldsymbol{X}_0, X_{kb}) = \frac{1}{2} \sum_{c=0}^{m-1} E_{ij}(\boldsymbol{X}_0, \kappa_{kc}) \exp(2\pi \mathrm{i}\ c\ b/m) \tag{35}$$

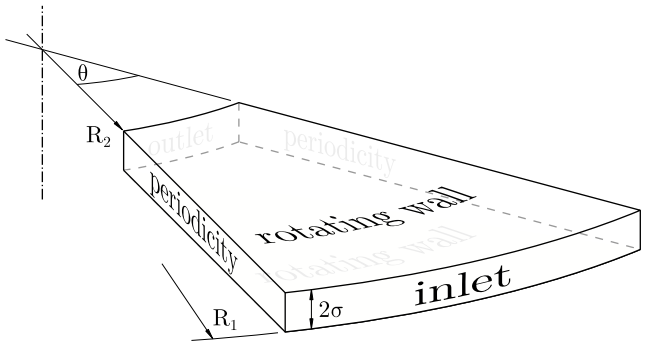

Fig. 3. Schematic view of the computational domain.
Source: Figure by Klingl [16].

Fig. 4. Visualization of the volume force in Z-direction that is applied to the fluid field at the planes $Z = 0$ (top) and $\phi = 0$ (bottom) at one point in time during run C1.

$$b = 0, 1, \dots, m-1. \tag{36}$$

Values of turbulent dissipation are collected during runtime of the simulation in nondimensional form by

$$\epsilon = \frac{\sigma}{2\,\mathrm{Re}}\overline{\left(\frac{\partial U_i'}{\partial j} + \frac{\partial U_j'}{\partial i}\right)\left(\frac{\partial U_i'}{\partial j} + \frac{\partial U_j'}{\partial i}\right)} \tag{37}$$

where the indices i and j each represent one of the coordinate directions r, ϕ, and z and summation over repeated indices is implied. Turbulent kinetic energy in nondimensional form is calculated by

$$K = \frac{1}{2}\overline{(U_r'^2 + U_\phi'^2 + U_z'^2)} \tag{38}$$

For modal analysis of the flow field, two dimensional discrete Fourier transforms are computed.

$$\mathcal{V}'(\boldsymbol{X}_0, \gamma_{kd}, \gamma_{le}) = \frac{1}{mn}\sum_{b=0}^{m-1}\sum_{c=0}^{n-1} V'(\boldsymbol{X}_0, X_{kb}, X_{lc}) \exp(-2\pi \mathrm{i}(d\ b/m + e\ c/n)) \tag{39}$$

$$d = 0, 1, \dots, m-1 \tag{40}$$

$$e = 0, 1, \dots, n-1 \tag{41}$$

V' is the fluctuating component of any of the velocity components or the pressure. Its values are extracted on a plane spanned by the k and l coordinate directions that intersects the point $\boldsymbol{X}_0$. Here, k and l can be either spatial coordinate or time. The Fourier coefficients $\mathcal{V}'$ are functions of the wavenumbers γ_k and γ_l, whereas the variables V' are functions of the coordinates X_k and X_l. The discrete coordinates X_{kb} and X_{lc} and wavenumbers γ_{kd} and γ_{le} relate to the respective series indices b, c, d and e in a similar manner as shown in Eqs. (33) and (34). For consistency with the linear stability investigations by Klingl et al. [5,12], temporal wavenumbers γ_t will be presented in the results sections with an inverted sign.

2.2. Geometry and domain

The domain of interest is a narrow annulus limited by two flat corotating surfaces in axial direction and cylindrical in- and outflow boundaries in radial direction. The dimensions of the annulus are chosen to resemble the test facility by Schosser [11], for which experimental velocity distributions are available. Fig. 3 shows a schematic overview. The computational domain does not cover the full circumference of the test facility annulus but rather a sector with rotationally periodic boundary conditions, spanning a certain angle θ. Table 1 lists the nondimensional domain geometries for all simulation runs as well as the dimensional test facility geometry that the nondimensional parameters are based on.

2.3. Mesh

The domain is covered by a regular, cylindrical mesh, constituted of approximately cubic spectral elements. Each element is internally resolved with a polynomial order of seven in each spatial direction, which is the recommended polynomial order for Nek5000 [15]. The element height has a small linear growth normal to the disks, to make the elements adjacent to the disks flatter. Table 2 summarizes the mesh sizes of all simulation runs.

2.4. Boundary conditions

The disk surfaces are modelled as corotating no slip walls. In radial direction, there is a velocity inlet boundary at R_1 and an outlet boundary at R_2. To match the numerical simulations to experimental operating conditions by Schosser [11], the radial mass flow is approximated from averaged experimental radial velocities and density estimates based on measured temperature and pressure data during experiment. The flow angle at the inlet is also approximated from the experimental velocity distributions.

The circumferential boundaries are rotationally periodic. Initial conditions as well as the inlet boundary condition are calculated from an analytical model of the inter-disk flow from simplified Navier–Stokes equations with velocity profiles assumed to be axisymmetric and parabolic. The model is based on ideas by Beans [2]. Table 3 summarizes the operating conditions. The mass flow values $\dot{m}$ refer to the mass flow thorough the full disk gap, not just the periodic sector covered by the simulation.

Directly downstream of the inlet boundary, a random body force is imposed in the direction normal to the disks, to disturb the flow and possibly trigger transition. The forcing is implemented after Schlatter and Örlü [18] and consists of a superposition of a specified number of radial and circumferential modes with unity amplitude and a random phase shift ξ_{abc} between 0 and 2π.

$$h_a(R, \phi) = \frac{1}{m}\sum_{b=b_{min}}^{b_{max}}\sum_{c=c_{min}}^{c_{max}} \sin(bR\gamma_{r0} + c\phi\gamma_{\phi 0} + \xi_{abc}) \tag{42}$$

$$m = (b_{max} - b_{min} + 1)(c_{max} - c_{min} + 1) \tag{43}$$

The random number generator that determines ξ_{abc} is tied to simulation time, so that the random numbers between simulations are the same and runs can be restarted smoothly. The wavenumbers in radial and circumferential directions are multiples of the base wavenumbers γ_{r0} and $\gamma_{\phi 0}$. m is the total number of modes. In circumferential direction, only modes that fit into the domain according to the rotationally periodic boundary conditions are taken into account. In time, the forcing changes smoothly between different random versions of h_a. The "floor(x)"-function takes any real argument x and rounds it down to the nearest integer smaller than or equal to x.

$$a(T) = \mathrm{floor}\left(\frac{T}{\Delta T}\right) \tag{44}$$

$$g_0(T) = \frac{T}{\Delta T} - a(T) \tag{45}$$

Table 1
Domain dimensions for the computations.

Run		A1	A2	B1	B2	B3	B4	B5	B6	C1
R_1	–	1	1	1	1	1	1	1	1	1
R_2	–	0.467	0.467	0.467	0.467	0.467	0.467	0.333	0.467	0.789
σ	–	0.00333	0.00333	0.00333	0.00333	0.00333	0.00333	0.00333	0.00333	0.00439
θ	°	30	30	30	30	30	45	30	30	3.6
r_1	mm	75	75	75	75	75	75	75	75	57
r_2	mm	35	35	35	35	35	35	25	35	45
s	mm	0.25	0.25	0.25	0.25	0.25	0.25	0.25	0.25	0.25

Table 2
Number of spectral elements used in the simulation meshes.

Run	A1	A2	B1	B2	B3	B4	B5	B6	C1
n_r	480	480	480	560	400	480	600	480	648
n_ϕ	347	347	347	382	333	520	347	347	171
n_z	6	6	6	7	5	6	6	6	27
n	999 360	999 360	999 360	1 497 440	666 000	1 497 600	1 249 200	999 360	2 991 816

Table 3
Operating conditions for the computations. Expected flow regime is either laminar (lam.), transitional (tra.) or turbulent (tur.).

Run		A1	A2	B1	B2	B3	B4	B5	B6	C1
$\dot{m}$	g/s	3.12	3.12	6.91	6.91	6.91	6.91	6.91	6.91	12.7
$\hat{u}_{r1}$	m/s	11.5	11.5	24.2	24.2	24.2	24.2	24.2	24.2	44.6
ω	1/s	104.7	104.7	104.7	104.7	104.7	104.7	104.7	104.7	523.6
ρ	kg/m^3	1.15	1.15	1.21	1.21	1.21	1.21	1.21	1.21	1.59
μ	µPa s	18.2	18.2	18.2	18.2	18.2	18.2	18.2	18.2	18.2
α_1	°	44	44	50	50	50	50	50	50	31
Re	–	182	182	403	403	403	403	403	403	974
Ta	–	124	124	131	131	131	131	131	131	652
regime		lam.	lam.	tra.	tra.	tra.	tra.	tra.	tra.	tur.

Table 4
Inlet region body force parameters.

Run	A1	A2	B1	B2	B3	B4	B5	B6	C1
λ_t	1000	10 000	10	10	10	10	10	1000	10 000
γ_{r0}	1	1	1	1	1	1	1	1	1
b_{min}	−1000	−1000	−1000	−1000	−1000	−1000	−1000	−1000	400
b_{max}	1000	1000	1000	1000	1000	1000	1000	1000	1000
$\gamma_{\phi 0}$	12	12	12	12	12	8	12	12	100
c_{min}	1	1	1	1	1	1	1	1	1
c_{max}	100	100	100	100	100	100	100	100	20

$$g_1(T) = 3g_0(T)^2 - 2g_0(T)^3 \tag{46}$$

$$g_2(T, R, \phi) = (1 - g_1(T))h_a(R, \phi) + g_1(T)h_{a+1}(R, \phi) \tag{47}$$

The forcing is multiplied with a Gaussian distribution to restrict it to a few percent of the radial domain length right after the inlet boundary. The parameter λ_t is there to adjust the intensity of the forcing.

$$\boldsymbol{F}_t(T, R, \phi, Z) = \boldsymbol{e}_z \ \lambda_t \ g_2(T, R, \phi) \exp\left(-\left(\frac{R - R_{0t}}{L_{rt}}\right)^2 - \left(\frac{Z - Z_{0t}}{L_{zt}}\right)^2\right) \tag{48}$$

Table 4 summarizes the ranges of imposed radial and circumferential modes as well as the strength parameter for each simulation run.

In the outlet region, there is a sponge region, implemented after Chevalier et al. [19], where a second body force is applied that forces the flow back to the parabolic solution $\boldsymbol{U}_{ic}$. The region is restricted to approximately five percent of the radial domain length just upstream of the outlet by multiplication with a smooth step function. The intensity of the dampening can be adjusted with the parameter λ_d.

$$R_d = \frac{R - R_{0d}}{L_{rd}} \tag{49}$$

$$q(R_d) = \begin{cases} 0 & \text{for } R_d \geq 1 \\ (1 + \exp(-\frac{1}{R_d - 1} - \frac{1}{R_d}))^{-1} & \text{for } 0 \leq R_d \leq 1 \\ 1 & \text{for } R_d \leq 0 \end{cases} \tag{50}$$

$$\boldsymbol{F}_d(T, R, \phi, Z) = \lambda_d \ q(R_d)(\boldsymbol{U}_{ic}(T, R, \phi, Z) - \boldsymbol{U}(T, R, \phi, Z)) \tag{51}$$

Fig. 4 shows the imposed forcing at one point in time during the simulation run C1 on two slices of the simulation domain. Both the inlet perturbation and the outlet dampening are visible.

For comparison with results later on, Fig. 5 shows the two-dimensional Fourier analysis of the inlet perturbation during run B1. The figures show the forcing F_z on two-dimensional slices in space and time, together with the corresponding Fourier transform $\mathcal{F}_z$ according to Eq. (39). The forcing evenly covers rectangular areas in the frequency planes, where the spatial wavenumber limits from Table 4 can be observed. In time, the forcing covers wavenumbers between approximately −500 and 500.

2.5. Software and hardware

Fluid simulations are conducted using the open source solver Nek5000 [15]. It employs a spectral element method to solve the Navier–Stokes equations for an incompressible fluid. For all computations in this study, the Pn-Pn formulation is selected, time is advanced through third order backward differentiation with a CFL number of 0.5. All filtering is turned off.

At each time step during runtime, averaging of velocities, pressure, Reynolds stresses, wall shear stress and fluctuating rate of strain tensor (see Eq. (37)) is performed. Full snapshots of the fluid field are saved in certain intervals of simulation time. In addition to that, the fluid field is interpolated onto a more coarse, regular mesh for Fourier analysis and saved with a higher output frequency than for the full snapshots. During postprocessing, visualizations of the flow fields are generated by VisIt (refer to Childs et al. [20]). All other analysis, for example Fourier analysis and two-point correlations, are calculated and visualized through custom implementations in Mathematica [21]. Computations are performed on SuperMUC-NG at the Leibniz-Rechenzentrum in Garching, Germany. 35 million core hours were granted for the project, computation jobs utilized up to 50000 compute cores in parallel.

2.6. ANSYS CFX fluid simulation setup

For comparison of the results to commercial fluid simulation software, an accompanying computation is set up in ANSYS CFX [22]. It covers the same domain size and operating conditions as the direct

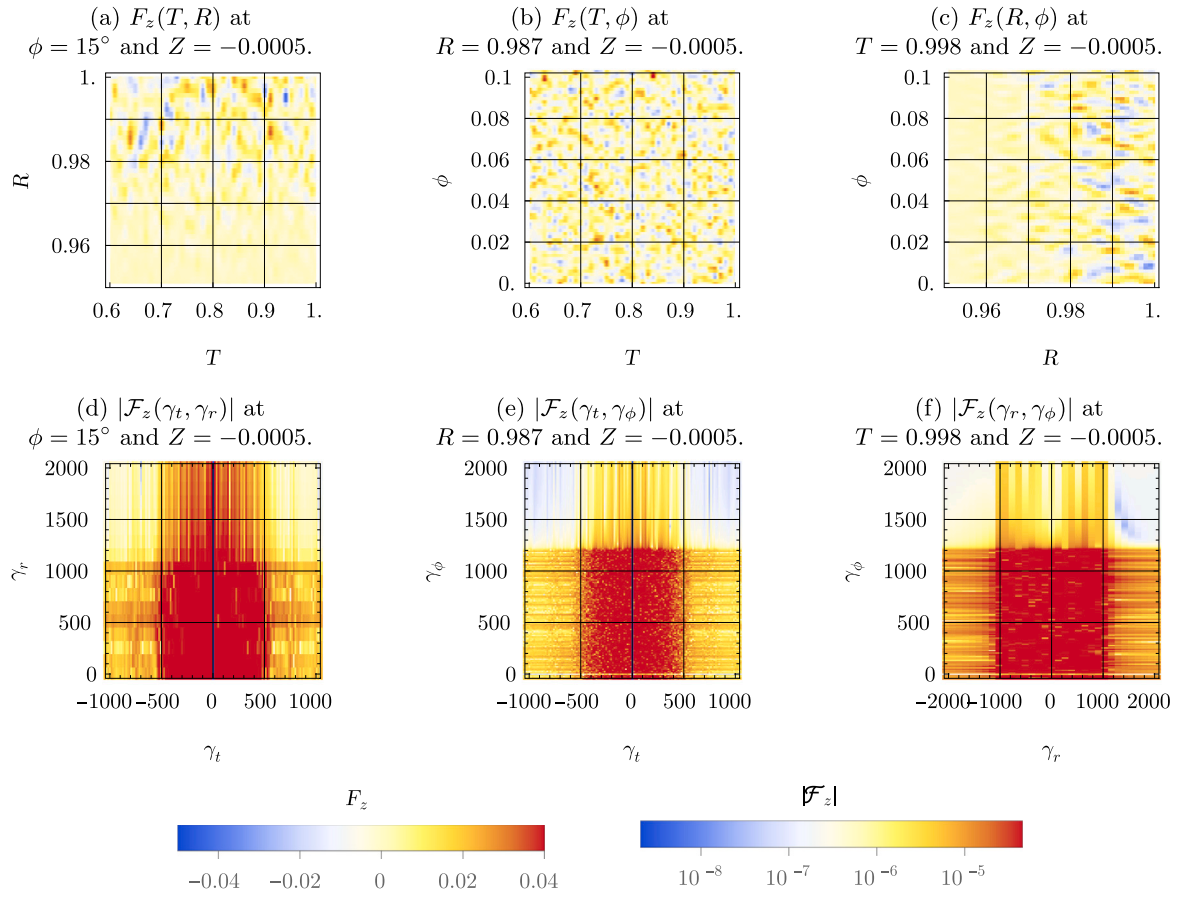

Fig. 5. Fourier analysis of the inlet forcing during run B1, across two-dimensional slices of the simulation domain in time and space. (For interpretation of the references to colour in this figure legend, the reader is referred to the web version of this article.)

numerical simulations from Tables 1 and 3, only the circumferential extent of the domain is restricted to $\theta = 1°$. The medium is incompressible air. In terms of turbulence modelling, the SST model is enabled for the turbulent operating conditions (C) and the Gamma-Theta transitional turbulence model is active for the transitional operating conditions (B). Medium turbulence intensity is specified at the inlet boundary. Laminar conditions (A) are simulated without turbulence modelling. At the inlet, parabolic velocity profiles are specified, consistent with the DNS inlet boundary condition. The outlet boundary has a given pressure level. Walls are rotating and rotational periodicity is specified at the circumferential boundaries. A regular mesh is employed, with decreasing element size towards the rotating walls and towards the inlet and outlet. A mesh independence study is set up for the turbulent operating conditions of run C1, to determine an appropriate mesh resolution. Three meshes with varying number of elements in all spatial directions are compared. As indicator variables, velocity, turbulent kinetic energy and turbulent dissipation profiles at $R = 0.825$ are chosen. The results from the three meshes are visually almost indistinguishable, Fig. 6 shows the circumferential velocity profile as an example. The "medium" mesh with 158400 elements is selected for further analysis. It features 48 mesh elements between the disk surfaces and the mesh points closest to the walls below $Z^+ = 1.1$.

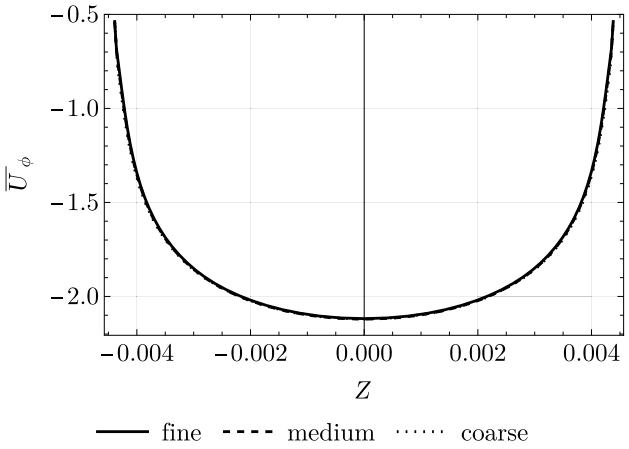

Fig. 6. Comparison of circumferential velocity profiles at $R = 0.825$ from ANSYS CFX simulations on fine (324 900 elements), medium (158 400 elements) and coarse (79 380 elements) meshes.

3. Mesh and domain size independence

Regarding the direct numerical simulation of laminar and transitional conditions, comparison of simulation runs B1 to B6 serves as mesh independence study to rule out mesh and domain boundary influence. The computations are set up with identical operating conditions, but with longer and wider domain, coarser and finer mesh as well as bigger perturbation amplitude compared to a reference case. For a visual comparison of the cases, Figs. 7 and 8 give close up views of the flow field and the corresponding spectra computed from Eq. (39). Only the spatio-temporal analysis of the radial velocity component in the T-R-plane is shown, because the other results for slices in other coordinate directions and for other velocity components and pressure agree equally well across all runs. The structures in Fig. 7(d) do not match

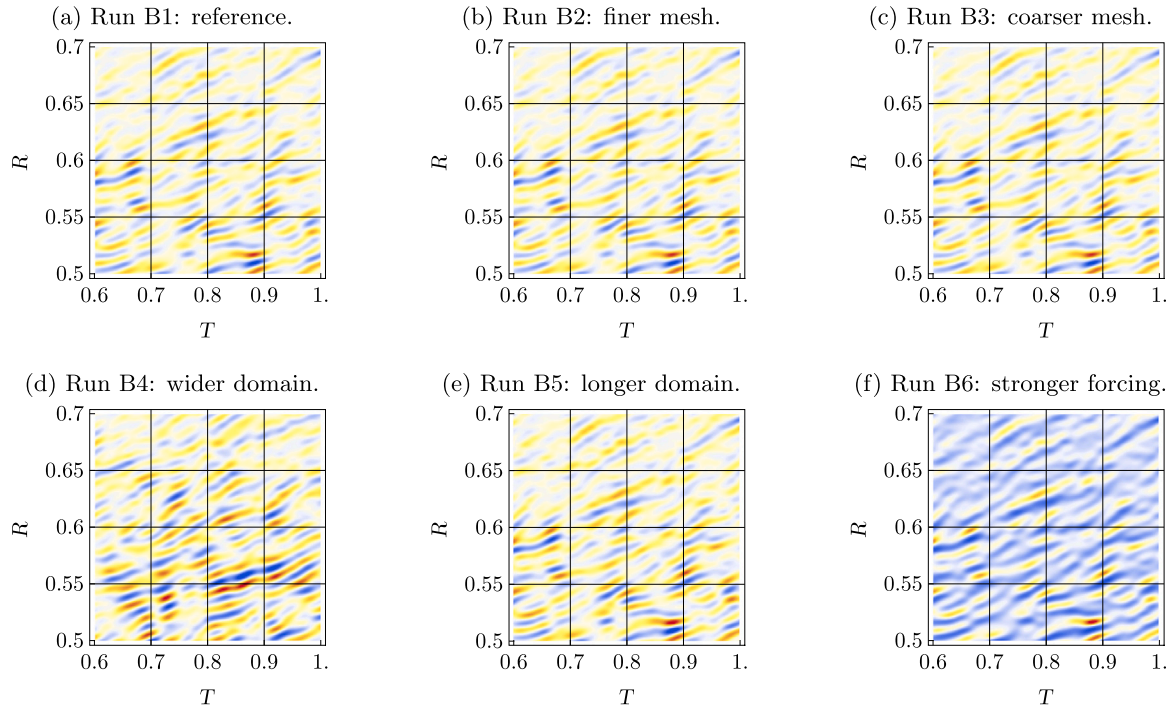

Fig. 7. Detail view of the fluctuating component U_r' of the radial velocity on a plane for constant $\phi = 15°$ and $Z = -0.0005$ across runs B1–B6. For the colour scales see Fig. 9.

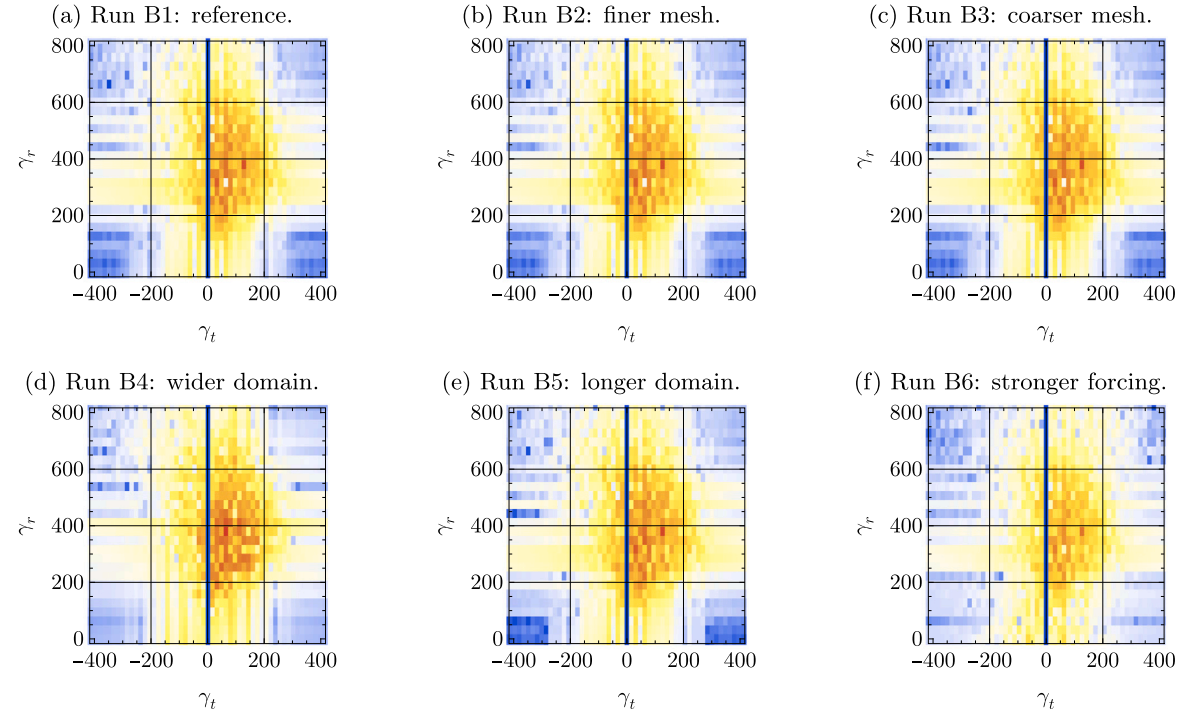

Fig. 8. Fourier transforms $|\mathcal{U}_r'|$ corresponding to Fig. 7 across runs B1–B6. The colours show absolute values of the Fourier coefficients on a logarithmic scale. For the colour scales see Fig. 9.

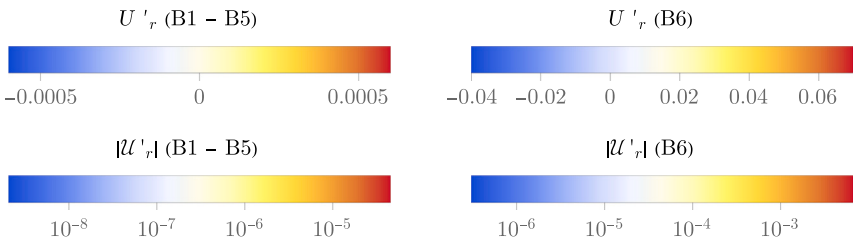

Fig. 9. Colour scales for Fourier analysis of simulation runs B1–B6. (For interpretation of the references to colour in this figure legend, the reader is referred to the web version of this article.)

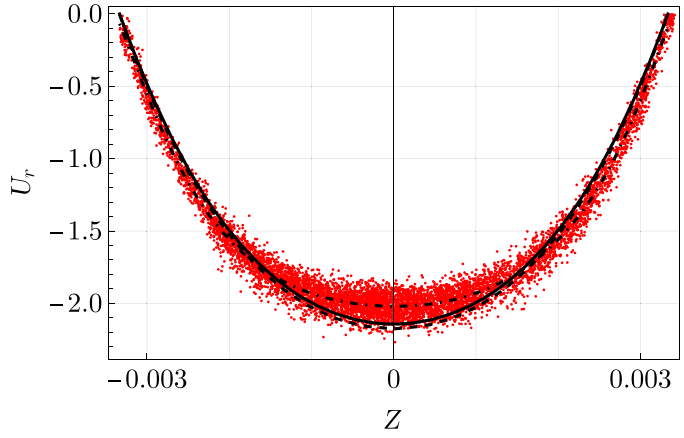

(a) Radial laminar velocity profiles.

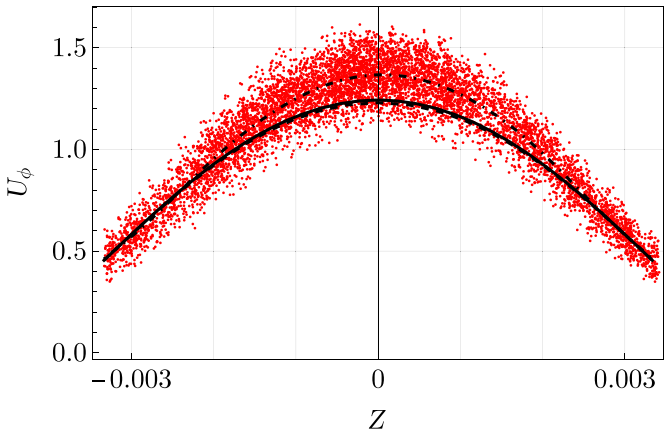

(b) Circumferential laminar velocity profiles.

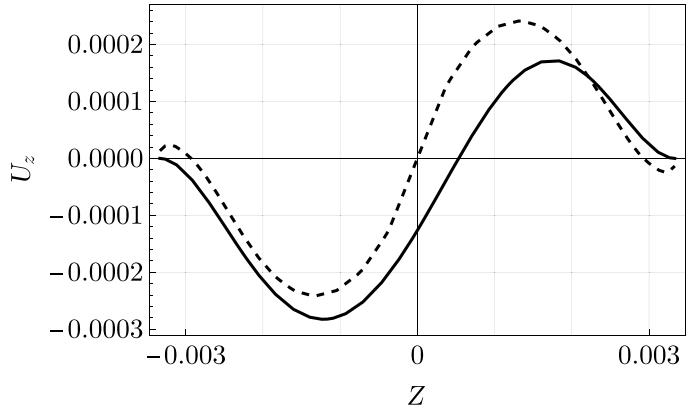

(c) Axial laminar velocity profiles.

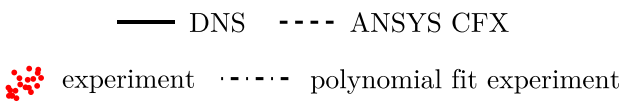

Fig. 10. Velocity profile comparison during run A1 at $R = 0.6667$. Experimental data was recorded by Schosser [11].

the other cases because for the wider domain, other circumferential modes are imposed. This influences the phase shift of the radial modes as well, because the state of the random number generator is affected. Looking at the spectral analysis in Fig. 8 however, the dominant modes are consistent with the other runs.

4. Laminar simulations (cases A1 and A2)

This section describes results from the two laminar runs A1 and A2. They differ in the strength of the perturbation forcing, which is increased by a factor of 10 for run A2. The results from the two runs turned out very similar, except for the amplitude of the unsteady flow structures. Because of this, this section only displays results from run A1.

Velocity profiles from DNS, ANSYS CFX and experiment are compared by Fig. 10. There is a slight mismatch in the radial velocity between numerical data and experiment since there is some inaccuracy in the estimation of air density and mass flow from the measurements. The circumferential velocity component on the other hand is underestimated to a small degree. Furthermore, the DNS flow field is not entirely stationary because of the artificial perturbation. This does not visibly alter radial and circumferential velocity profiles because of the small perturbation amplitude, it does however result in asymmetry of the axial velocity profile at the particular point in time that is captured in the figure.

Fig. 11 shows the Fourier analysis of a slice of the fluid domain in radial direction and in time for constant axial and circumferential coordinates. The forced perturbation in the inlet region, right after

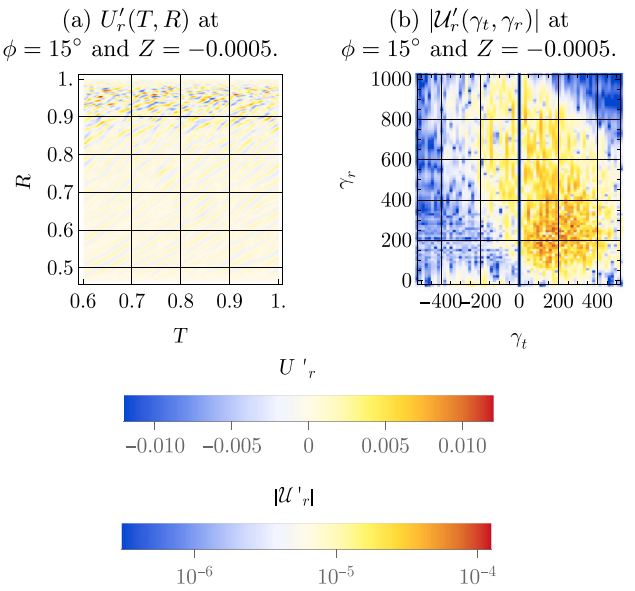

Fig. 11. Fourier analysis of the fluctuating component of radial velocity U'_r during run A1. (For interpretation of the references to colour in this figure legend, the reader is referred to the web version of this article.)

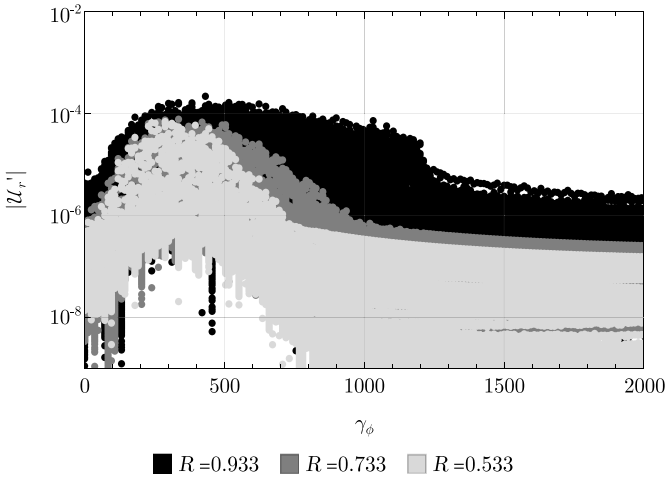

Fig. 12. Radial development of perturbation amplitude during run A1. The chart shows the two-dimensional Fourier transform of the radial velocity on T-ϕ-slices through the domain at $Z = -0.0005$ and different radial positions. The slices cover a timespan from $T = 0.6$ to $T = 1$. Temporal wavenumbers are not distinguished.

$R = 1$ is visibly dampened with decreasing radius towards the outlet. The spectral plot on the right-hand side can be compared to the broad spectrum of artificially induced modes from Fig. 5 between $\gamma_t = \pm 500$ and between $\gamma_r = 0$ to $\gamma_r = 1000$. It becomes apparent that some modes are dampened faster than others.

A clearer visualization of the radial development of the fluctuation amplitude is depicted by Fig. 12. Here, the two-dimensional Fourier transforms of T-ϕ-slices of the domain, each with constant radial and axial coordinates are shown for different radii. It can be seen that the induced fluctuations are dampened across the whole range of circumferential wavenumbers for decreasing R. In a region around $\gamma_\phi = 300$, the dampening is very weak. This is consistent with the location of the laminar operating conditions in the stability plane, shown in Fig. 2, close to the stability boundary, but mostly in the stable region. The weak dampening rate of some perturbation wavelengths is a possible explanation for the spread of experimental data points in Fig. 10, which is larger than the estimated measurement uncertainty of ±4.1 %

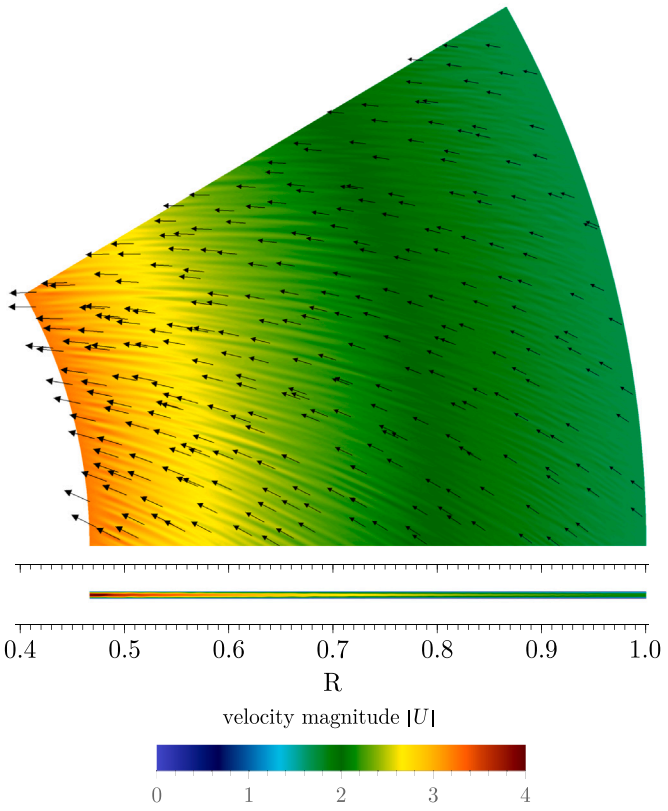

Fig. 13. Velocity magnitude on a colour scale and velocity vectors on planes at $Z = 0.0050$ (top) and $\phi = 0$ (bottom) from computation B6. (For interpretation of the references to colour in this figure legend, the reader is referred to the web version of this article.)

by Schosser [11]. Certain unsteady flow structures that develop in the nozzle or during transition between nozzle and rotor might remain in the flow throughout the rotor even if the flow is theoretically stable.

5. Onset of instability (cases B1 to B6)

5.1. Flow visualization and Fourier analysis

Fig. 13 visualizes the velocity magnitude and flow direction on a plane at 75 % of the domain height in Z-direction at a point in time at transitional operating conditions.

The bottom part of the figure shows a ϕ-normal slice to scale, to visualize the small aspect ratio of the gap. The plot is based on simulation run B6, which features a stronger inlet perturbation so that the flow oscillations are actually visible. In the other runs B1–B5, the oscillations caused by the inlet perturbation are so small, that they visually vanish in the velocity magnitude plot.

A comparison of velocity profiles at the same radial position as previously in the laminar case is displayed in Fig. 14. The experimental velocity profiles now show a pronounced flattened centre in the radial component, together with a larger spread of data points than before. Since the conditions in theory are only weakly unstable, close to the theoretical stability boundary, it seems likely that the flat region in the experimental profile is a consequence of strong perturbations that originated before or during entry of the flow into the disk gap. Because the imposed perturbation in the DNS is of very small amplitude, the DNS velocity profiles are essentially laminar profiles. In contrast, the Gamma-Theta transitional turbulence model in ANSYS CFX captures the experimental circumferential velocity profile quite well. In radial direction however, the CFX results resemble more the quasi-laminar

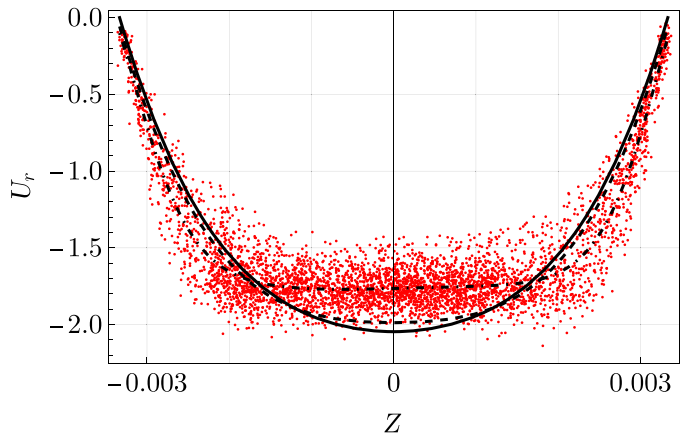

(a) Radial velocity profiles.

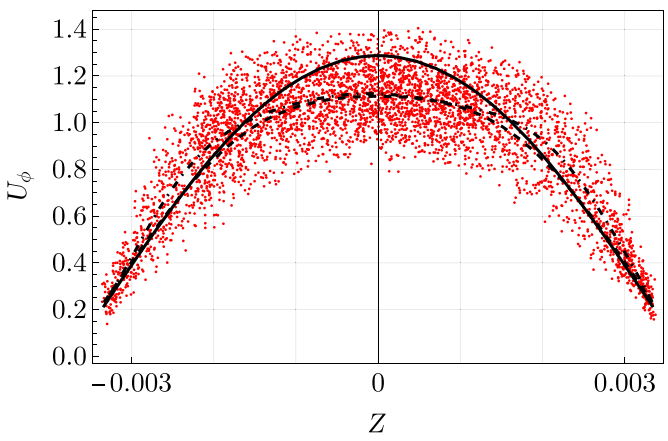

(b) Circumferential velocity profiles.

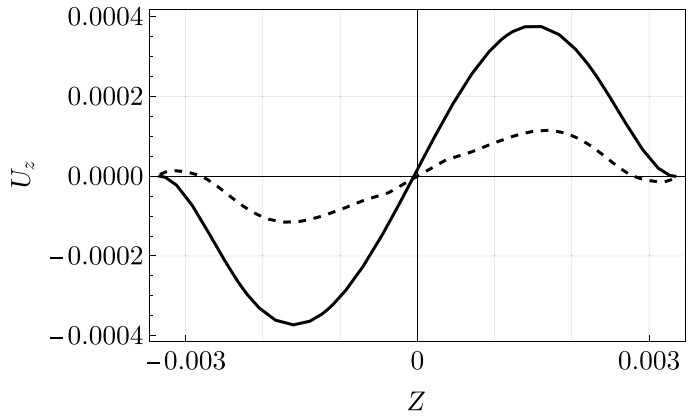

(c) Axial velocity profiles.

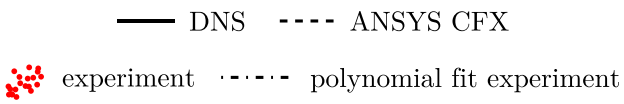

Fig. 14. Velocity profile comparison during run B1 at $R = 0.6667$. Experimental data was recorded by Schosser [11].

DNS results. Two reruns of the transitional CFX case, one with standard SST turbulence modelling and one without turbulence modelling, resulted in an underestimated and overestimated circumferential velocity component respectively.

For further characterization, Fig. 15 shows Fourier analyses in two-dimensional slices through the simulation domain in radial and circumferential direction, over a simulation time period from 0.6 to 1. All three slices are located at a constant Z coordinate at $Z = -0.0005$, close to the centre plane between the rotating disk surfaces. Only the analysis of the radial velocity component is shown because the other flow field components have a similar spectral structure. The T-R-plot and the R-ϕ-plot exhibit a rising perturbation amplitude in radial inward direction. The corresponding spectral plots in the lower half of the figure show the Fourier coefficients calculated according to Eq. (39). Again, they can be compared to the spectra of the imposed perturbation from Fig. 5. Most of the imposed modes are dampened, some of them are amplified.

Fig. 17 shows the radial development of the T-ϕ-Fourier coefficients more clearly, in a similar manner as previously for the laminar conditions in Fig. 12, but with reversed colours for clarity. Again, the absolute value of the Fourier coefficients is shown, from a two-dimensional Fourier transform of the fluctuating part of radial velocity, on slices for different constant values of R and Z as function of the circumferential wavenumber. As the flow progresses towards smaller radii, wavenumbers around $\gamma_\phi = 350$ get amplified by the flow, the rest is dampened.

5.2. Comparison to linear stability analysis

Fourier analysis of the DNS flow field also allows to verify results from linear stability analysis by Klingl et al. [12], which are based on the same domain geometry and operating conditions. Fig. 16 shows a comparison of the spectral maps and the unstable modes from the local linear stability analysis. The approach is termed “local” because it assumes radial homogeneity of the flow and is thus limited to a certain radial position. For comparison to the DNS results, the radial extent of the slices for Fourier analysis is limited to a small range surrounding the radial position of the local approach, which in this case is $R = 0.733$. The unstable modes predicted by linear stability analysis agree with the DNS results in terms of spatial wavenumbers, but slightly disagree in temporal wavenumber for some modes. Also, some of the points in the wavenumber planes that were probed by local linear stability analysis lie in the amplified region from the DNS spectra but showed up as stable in the linear analysis.

The remaining inconsistency between local linear theory and DNS is most likely a consequence of the assumption of radial homogeneity in the former analysis. This is demonstrated in Fig. 18 by comparison of DNS results and biglobal linear stability results by Klingl et al. [12]. The biglobal approach takes the radial development of the flow into account and yields circumferential and temporal wavenumbers of stable and unstable modes, while the radial and axial coordinate directions are numerically resolved with two-dimensional eigenfunctions. The comparison shows that the unstable modes from linear theory now coincide very well with the amplified region in the spectral map and are consistent with Fig. 17.

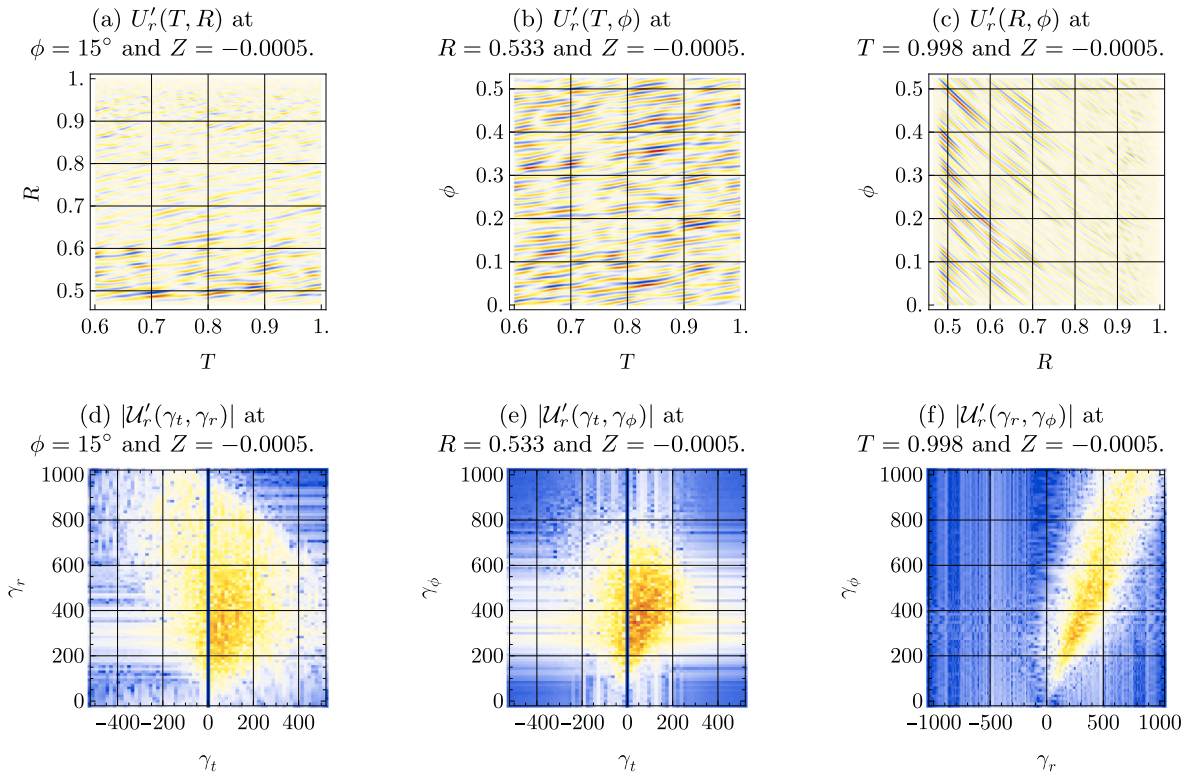

Fig. 15. Fourier analysis of the fluctuating component of radial velocity U_r' during run B1. For the colour scales see Fig. 9.

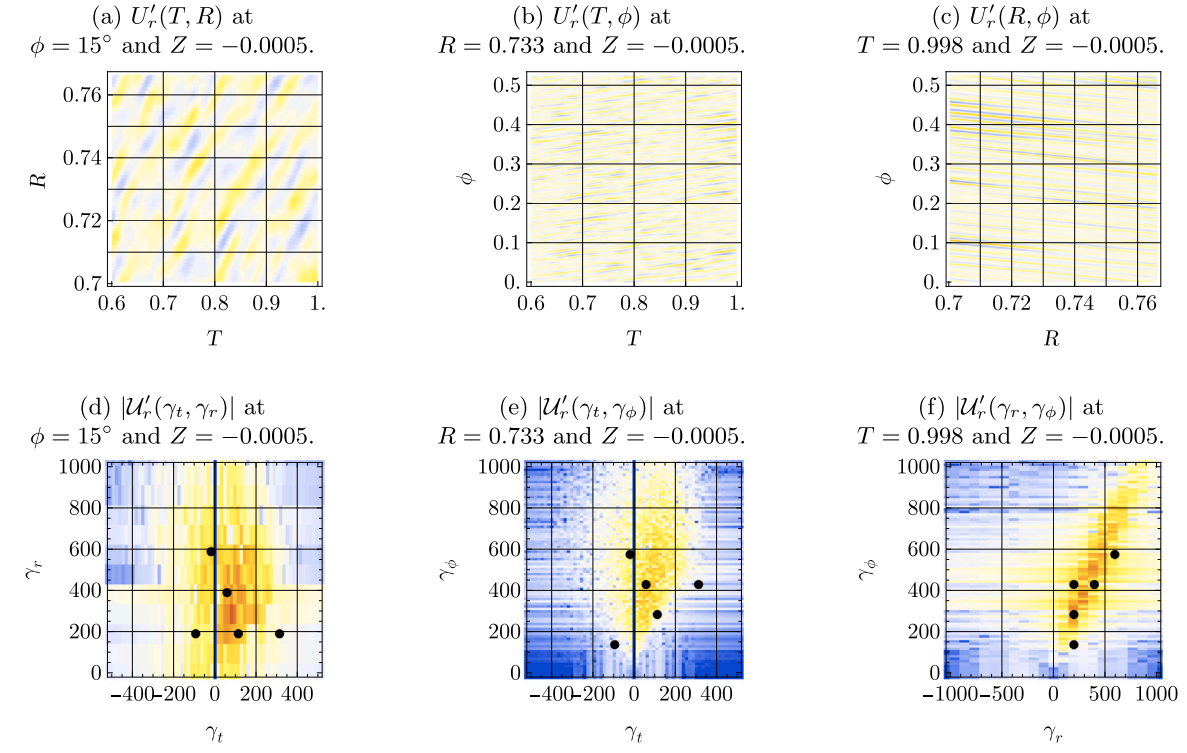

Fig. 16. Fourier analysis of the fluctuating component of radial velocity U_r' during run B1. The black dots are unstable modes found in the local linear stability analysis by Klingl et al. [12]. For the colour scales see Fig. 9.

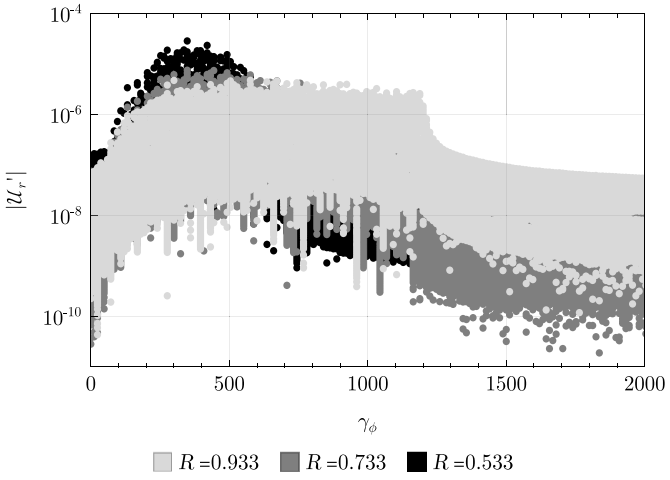

Fig. 17. Radial development of perturbation amplitude during run B1. The charts show the two-dimensional Fourier transform of T-ϕ-slices at $Z = -0.0005$ and different radial positions. The slices cover a timespan from $T = 0.6$ to $T = 1$. Temporal wavenumbers are not distinguished.

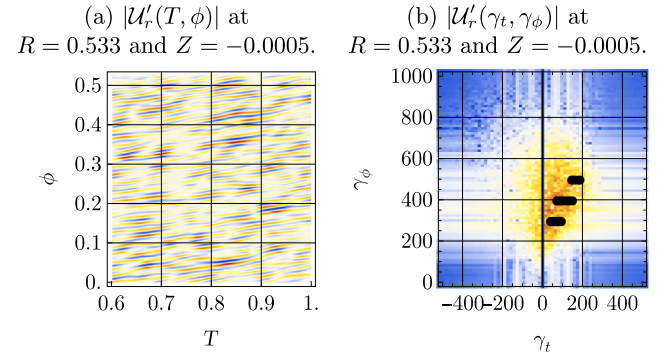

Fig. 18. Fourier analysis of the fluctuating component of radial velocity U_r' during run B1. The black dots are unstable modes found in the biglobal linear stability analysis by Klingl et al. [12]. For the colour scales see Fig. 9.

6. Turbulent simulation (case C1)

For a visual impression of the turbulent operating conditions, Fig. 21 shows axial and circumferential slices of a snapshot of velocity magnitude during simulation run C1. Upon entering the domain on the right hand side of the figure, the flow is initially laminar and then passes a strong perturbation forcing that induces oscillations. Further downstream, these break down into a chaotic velocity field.

At the same point in simulation time, Figs. 22 and 23 visualize vortices in the flow field by showing three-dimensional isosurfaces of the λ_2-criterion. Apparently, the strong oscillation of the flow in the inlet region causes small vortices to develop close to the wall, which then grow towards the channel centre as they travel downstream. The density of vortices in the chaotic velocity field that develops from this is initially high around $R \approx 0.925$ and then decreases again and stays visually approximately constant between $R \approx 0.9$ and the outlet.

In the following sections, the turbulent flow field is further analysed along lines through the domain in R and Z-direction. Results generally look the same for different circumferential positions. Analysis of simulation run C1 is based on a total amount of 4.55 nondimensional simulation time units. This is enough for the fluid to travel through the domain more than 22 times at average radial velocity. It took about 2.3 million time steps for the solver to cover this timespan.

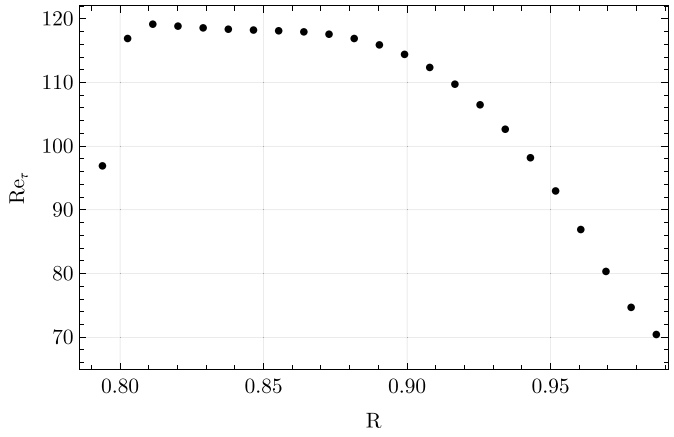

Fig. 19. Radial distribution of the friction Reynolds number Re_τ during run C1.

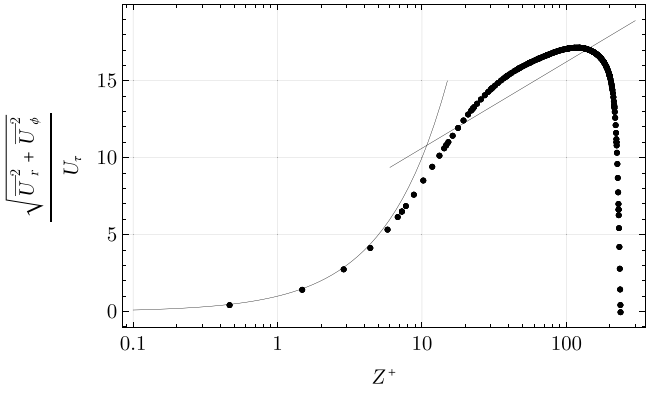

Fig. 20. Temporal average flow velocity in Z-direction at $R = 0.825$ and $\phi = 2.08°$, normalized with the friction velocity U_τ. The solid lines are $U_\tau = Z^+$ and $U_\tau = \frac{1}{0.41}\ln(Z^+) + 5$ [23].

6.1. Friction variables

For analysing friction variables, the domain is divided into 24 radial sectors, each with a width of 0.0088 nondimensional radial length units, which is equal to the axial distance between the rotating surfaces. In each of the sectors, the wall shear stress $\mathcal{T}_w$ is averaged during runtime of the simulation and friction velocity and friction Reynolds number are calculated using Eqs. (26) and (28). Fig. 19 shows friction Reynolds number for all radial sectors. After about half the radial domain length, Re_τ settles at values just below 120.

Fig. 20 compares the temporal average velocity magnitude, normalized with friction velocity, to the analytical law of the wall velocity profiles. There is good agreement in the viscous sublayer. In the centre of the channel, the numerical velocity profile overshoots the log-law. The black data points in the figure also show the distribution of mesh points close to the wall, with the closest point lying at $Z^+ = 0.466$. The local friction Reynolds number is $\mathrm{Re}_\tau = 118$, the width of the domain is 237 wall units.

6.2. Averaged quantities

The averaged quantities to be analysed in this section include average velocities, Reynolds stresses, turbulent kinetic energy and turbulent dissipation. These are collected during runtime of the simulation and can be compared to experiment and ANSYS CFX. Figs. 24 and 25 show velocity profiles from direct numerical simulation, experiment by Schosser [11] and from the reference case with active SST-turbulence modelling in ANSYS CFX. Apparently, simulation runtime

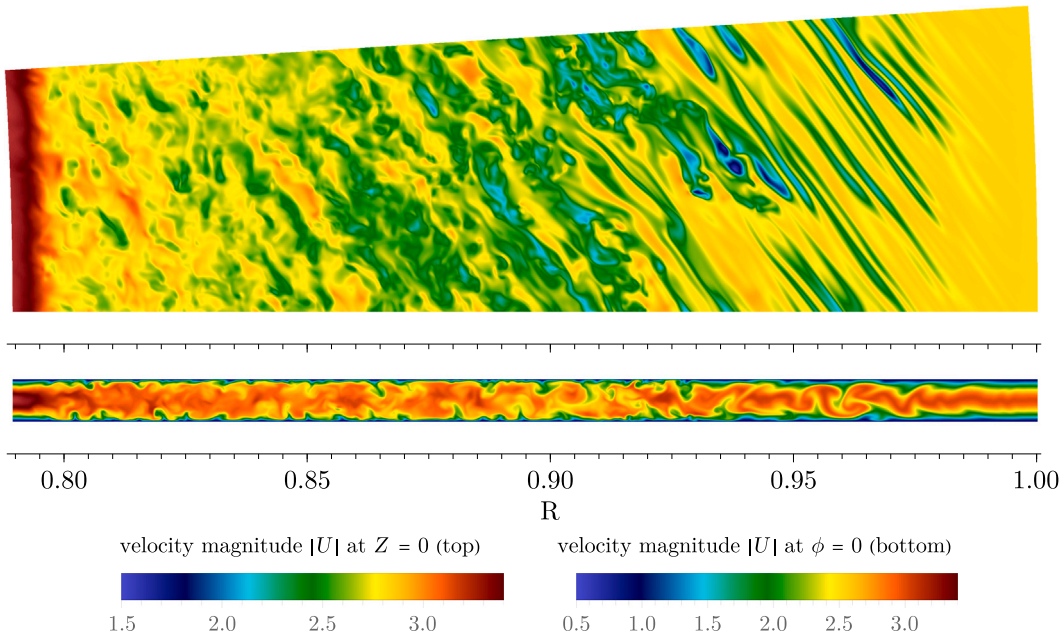

Fig. 21. Velocity magnitude at the planes $Z = 0$ (top) and $\phi = 0$ (bottom) at one point in time during simulation run C1. (For interpretation of the references to colour in this figure legend, the reader is referred to the web version of this article.)

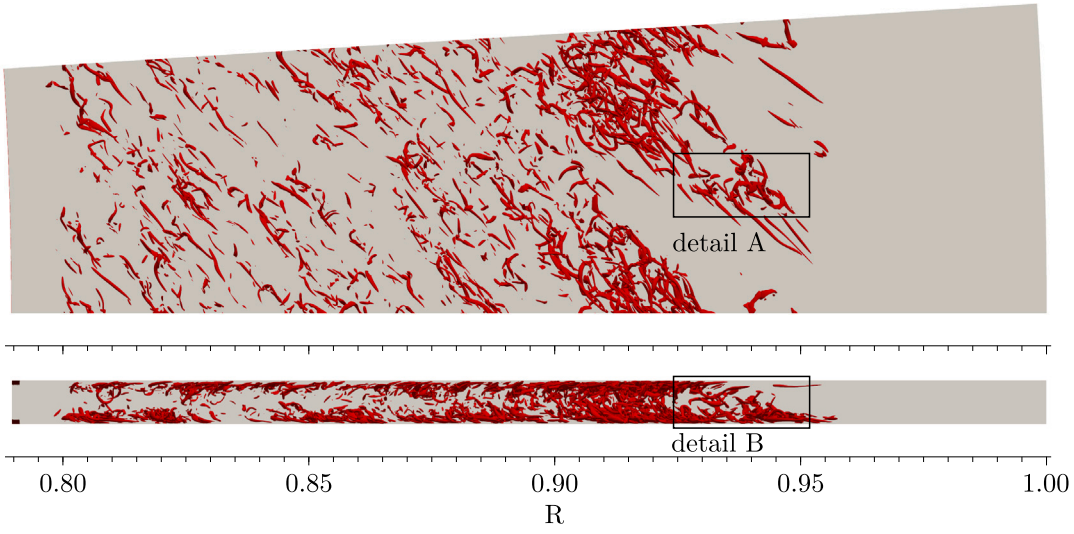

Fig. 22. Three-dimensional isosurfaces of the λ_2 criterion at $\lambda_2 = -100\,000$ at the same point in time as displayed in Fig. 21. Topview towards negative Z (top) and side view towards positive ϕ (bottom). For the detail views see Fig. 23.

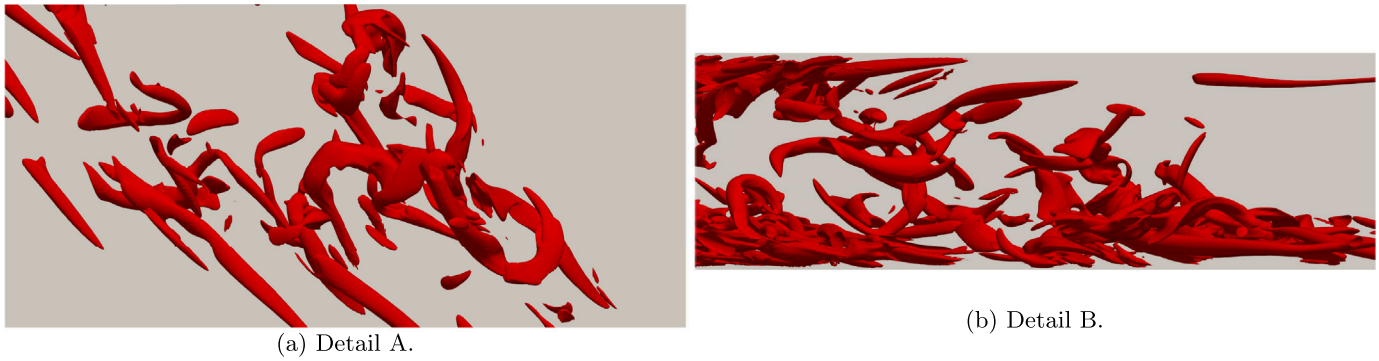

(a) Detail A.

(b) Detail B.

Fig. 23. Detail views indicated in Fig. 22.

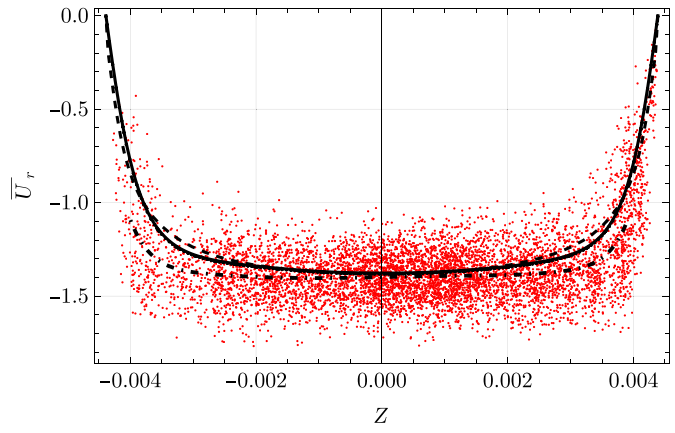

(a) Radial velocity profiles.

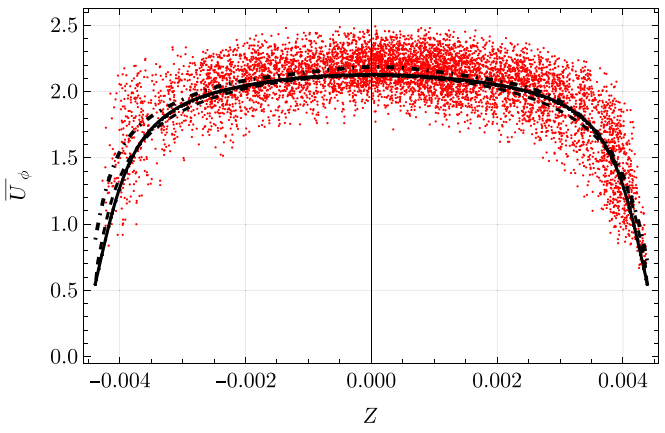

(b) Circumferential velocity profiles.

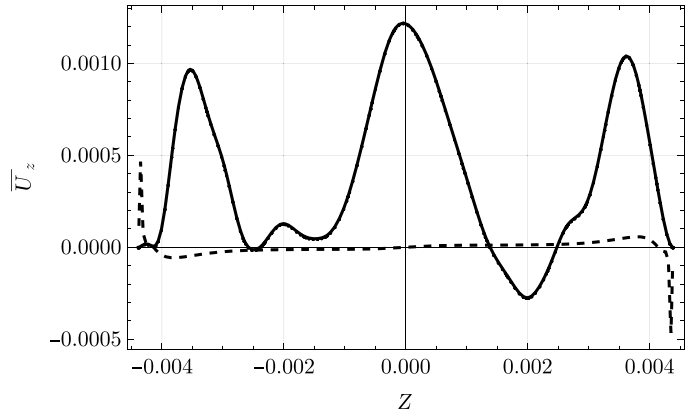

(c) Axial velocity profiles.

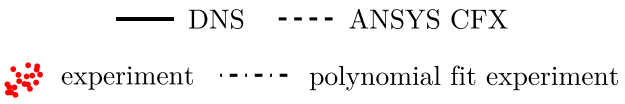

Fig. 24. Comparison of average velocity profiles from run C1 in axial direction at $R = 0.825$ and $\phi = 2.08°$. Experimental data was recorded by Schosser [11].

was not enough for the average axial velocity profile to reduce to zero. Compared to the instantaneous axial velocity profiles, its amplitude is however quite small.

For comparison, a 10th order polynomial is fitted to the experimental data points. All results agree very well. A rerun of the CFX computation with fluid compressibility does not change the results noticeably, however changing the inlet boundary condition from the custom parabolic velocity profile to the default rectangular bulk profile leads to a noticeable mismatch in circumferential velocity between the CFX results and DNS and experiment. The spread of the instantaneous velocity profiles from DNS matches the experimental data points in Fig. 25 very well.

Turbulent dissipation and turbulent kinetic energy along the axial direction are compared in Figs. 26(a) and 26(b) between ANSYS CFX and DNS. While the curves agree in the centre region of the channel, there is substantial deviation near the walls. The nondimensional Kolmogorov length scale based on the integral average of the DNS dissipation curve in Fig. 26(a) is 7.82×10^{-5}. The distance between mesh points is approximately equal to this measure in the centre of the channel and gets smaller towards the walls.

The distribution of those quantities along the radial direction, close to the centre of the disk channel, is displayed by Figs. 27(a) and 27(b).

Again, the radial development of the flow during DNS can be observed, with zero turbulence at the inlet boundary, then a rapid rise due to the perturbation and a slight decrease towards the outlet before turbulence is dampened away again. Naturally, DNS and CFX results disagree in the inlet region, but they approach each other towards smaller radii.

Figs. 28(a) and 28(b) show the diagonal and off-diagonal components of the Reynolds stress tensor from the DNS results. The magnitude of the tensor components is highest for the main flow directions R and ϕ.

6.3. Autocorrelations and energy spectra

Figs. 29 and 30 show the two point correlations of all three velocity components along the radial and circumferential direction, approximately in the centre between the disk surfaces.

The correlations are calculated according to Eq. (30). The run time of the simulation is not enough for the correlation functions to reduce to zero far away from the origin, but their general structure is already apparent. The width of the peaks at the origin is a measure for the size of turbulent structures. The X_ϕ-axis in Fig. 30 shows the arc length along the curve in circumferential direction, so it can directly be compared to the radial correlation. In radial direction, the axial velocity component develops smaller structures than the radial and circumferential component. In the circumferential correlation function, the circumferential velocity component of the structures appear to be larger than the radial and axial components.

The Fourier transforms of the two point correlations, calculated from Eq. (31), are displayed in Figs. 31 and 32. The Fourier coefficients E_{ij} cover more than 5 orders of magnitude and a section with a slope of $-5/3$ can very vaguely be made out. For wavenumbers larger than about 20 000 the spectra flatten out, which marks the lower limit of resolved structures.

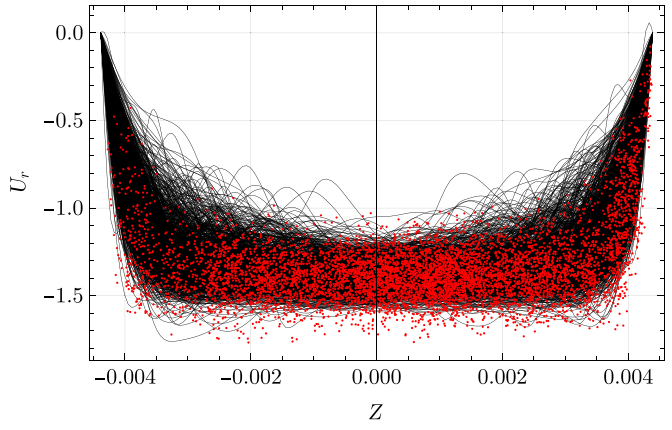

(a) Radial velocity profiles.

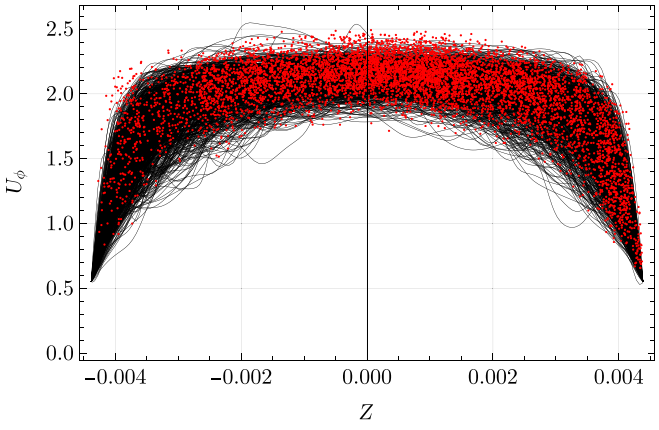

(b) Circumferential velocity profiles.

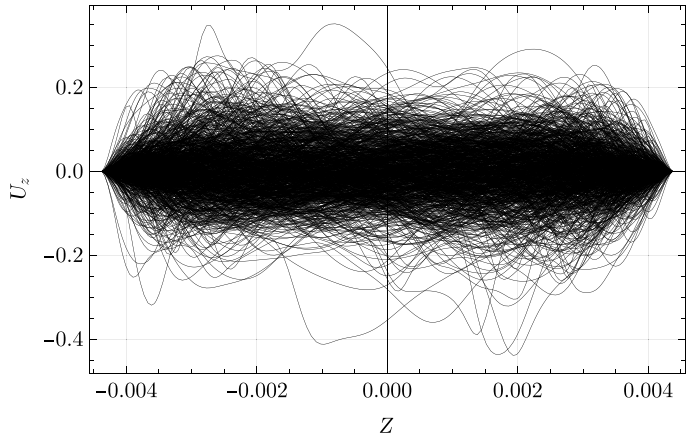

(c) Axial velocity profiles.

Fig. 25. Comparison of instantaneous velocity profiles from run C1 in axial direction at $R = 0.825$ and $\phi = 2.08°$.

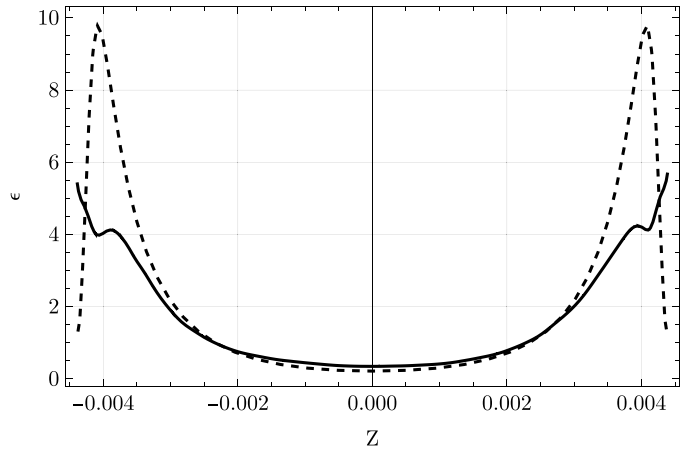

(a) Turbulent dissipation.

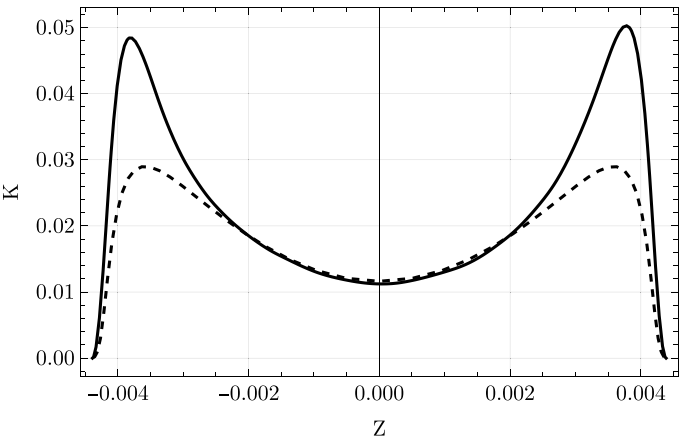

(b) Turbulent kinetic energy.

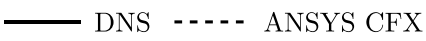

Fig. 26. Comparison of turbulent kinetic energy and dissipation profiles in axial direction at $R = 0.825$ and $\phi = 2.08°$.

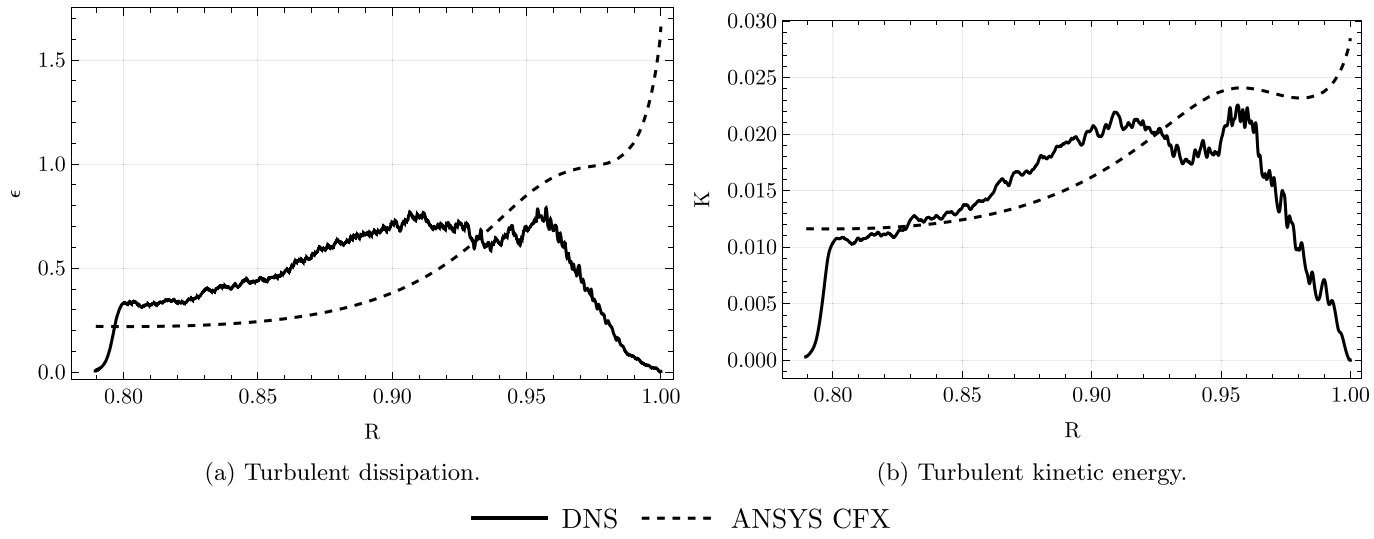

(a) Turbulent dissipation. (b) Turbulent kinetic energy.

Fig. 27. Comparison of turbulent kinetic energy and dissipation in radial direction at $Z = 0.000191$ and $\phi = 2.08°$.

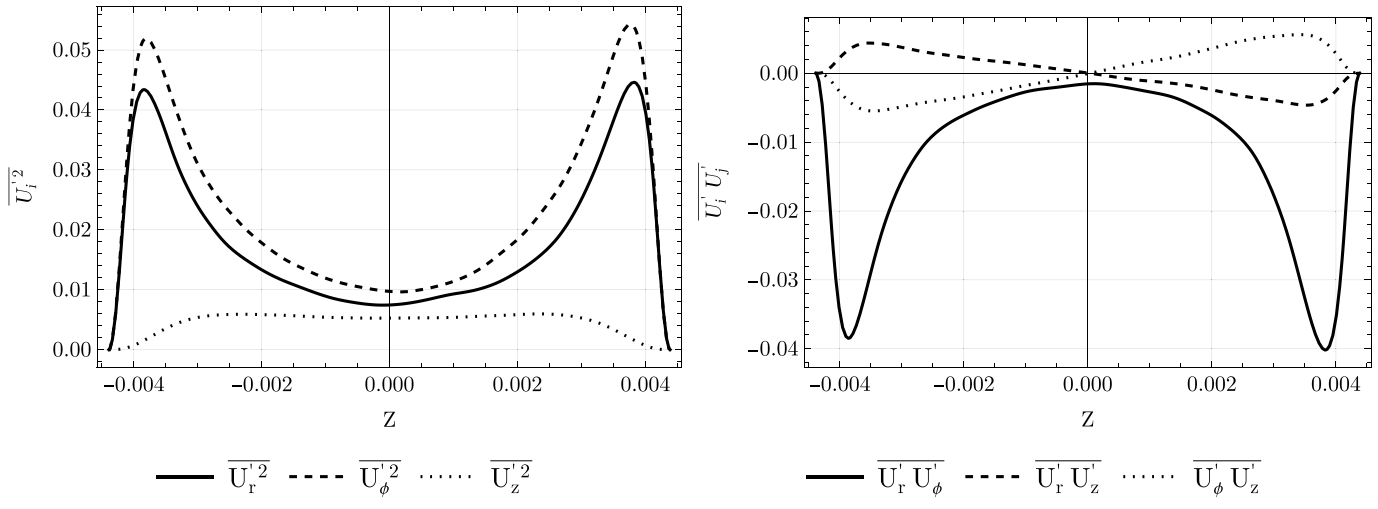

(a) Diagonal entries. (b) Off-diagonal entries.

Fig. 28. Reynolds stress tensor from DNS along the axial direction at $R = 0.825$ and $\phi = 2.08°$.

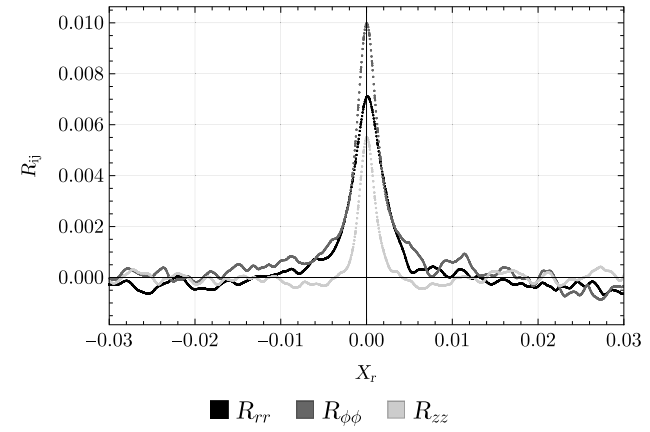

Fig. 29. Two point correlations in radial direction at $\phi = 2.08°$ and $Z = 0.000191$, the correlation origin $\boldsymbol{X}_0$ lies at $R = 0.825$.

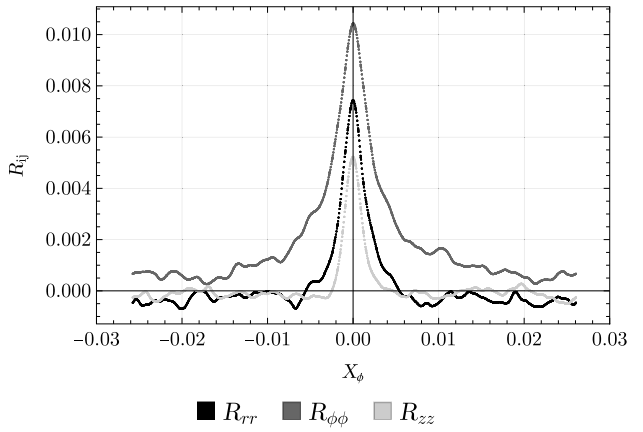

Fig. 30. Two point correlations in circumferential direction at $R = 0.825$ and $Z = 0.000191$, the correlation origin $\boldsymbol{X}_0$ lies at $\phi = 1.79°$.

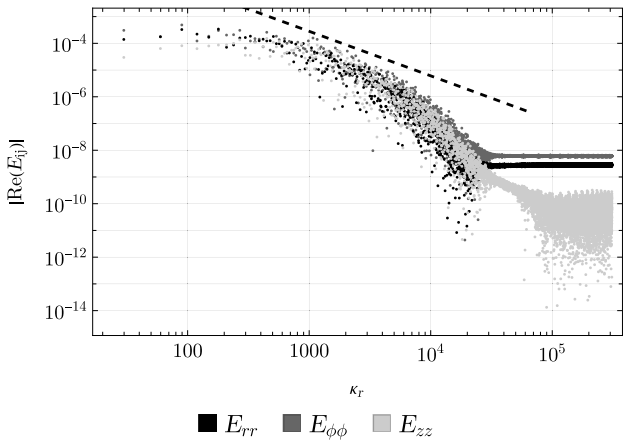

Fig. 31. Energy spectrum corresponding to Fig. 29. The dashed line has a slope of −5/3.

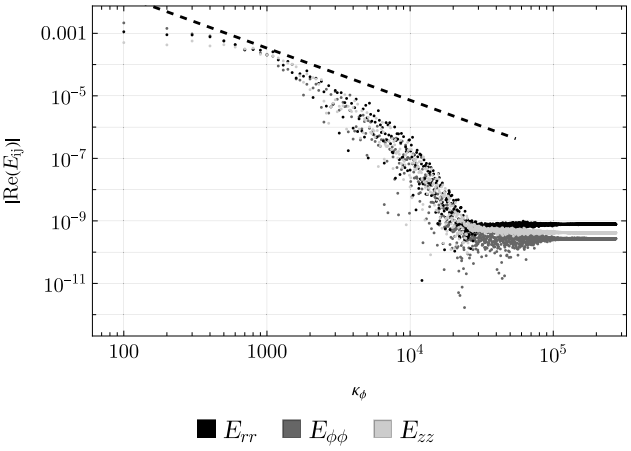

Fig. 32. Energy spectrum corresponding to Fig. 30. The dashed line has a slope of −5/3.

7. Conclusion

Radial inward flow between corotating disk for a geometry suitable for a friction turbomachinery application was examined using direct numerical simulation. The simulations cover sections of a flat annulus, with inlet and outlet boundaries in radial direction and rotating walls in axial direction. As operating conditions, three sets of parameters were chosen to reproduce the experimental conditions from the PTV measurements by Schosser [11]. When compared to the flow regime boundary from linear stability analysis by Klingl et al. [5], the three sets of parameters correspond to laminar, transitional and turbulent conditions.

For operating conditions corresponding to laminar flow, all imposed perturbations are shown to decrease in amplitude towards the outlet, with some modes however being dampened very slowly. At the transitional conditions on the other hand, a limited range of modes is amplified towards the outlet. The amplification is however quite small so that a transition to turbulence does not occur. Amplified modes from the DNS coincide with the modes that were previously identified to be unstable by Klingl et al. [5,12] through linear stability analysis. The linear stability approach with resolved axial and radial coordinates agrees better with DNS data than the local approach with assumed radial homogeneity.

For operating conditions leading to turbulent flow, velocity profile shapes between experiment by Schosser [11], DNS and a reference CFX case with SST turbulence modelling agree very well. It takes about half the radial domain length for turbulence to develop from the initial random perturbation. Turbulent kinetic energy and dissipation predictions from the CFX simulation agree with DNS data in the centre of the channel, but disagree near the walls. Two point correlations give an impression of the size of turbulent structures.

In conclusion, it was confirmed that transitional and turbulent flow structures have a convective nature and thus are strongly dependent on upstream perturbations. Instability that was observed in previous experiments at, or even below, the theoretical stability boundary is most likely a consequence of strong perturbation of the flow upon entering the disk gap during the experiments. Even if the flow is theoretically stable, the dampening rate of certain modes can be small, so that unsteady structures persist throughout the domain.

The present study is intended to serve as a reference and starting point for future computations. Transition mechanics and how they are affected by centrifugal and Coriolis effects require further investigation. Regarding the friction turbine application it would be interesting how transition and turbulence affects turbine performance. To generate more realistic inlet conditions, the domain could be extended radially outward to take into account the outer lateral surfaces of the disks to form a realistic disk gap inlet that can be supplied with a turbulent inlet boundary or a simulated nozzle.

CRediT authorship contribution statement

S. Klingl: Data curation, Formal analysis, Investigation, Methodology, Resources, Software, Validation, Visualization, Writing – original draft, Writing – review & editing. **S. Lecheler:** Project administration, Supervision, Writing – review and editing. **M. Pfitzner:** Conceptualization, Methodology, Project administration, Supervision, Writing – review and editing.

Declaration of competing interest

The authors declare that they have no known competing financial interests or personal relationships that could have appeared to influence the work reported in this paper.

Data availability

Data will be made available on request.

Acknowledgments

The authors gratefully acknowledge the Gauss Centre for Supercomputing e.V. (www.gauss-centre.eu) for funding this project by providing computing time on the GCS Supercomputer SUPERMUC-NG at Leibniz Supercomputing Centre (www.lrz.de).

Some visualizations displayed in this work have been produced via the VisIt remote GUI provided by the Leibniz Supercomputing Centre (LRZ) on the SuperMUC-NG system. We thank LRZ and its VisIt maintainer Dr. Salvatore Cielo for keeping this service optimized.

Michael Pfitzner would like to thank ITIS e.V. for financial support.

Appendix A. Symbols

Uppercase

E_{ij}	Nondimensional energy spectrum (–)
$\boldsymbol{F}$	Nondimensional body force vector (–)
$\boldsymbol{F_d}$	Imposed dampening forcing (–)
$\boldsymbol{F_t}$	Imposed perturbation forcing (–)
$\mathcal{F}_z$	Fourier transform of axial component of imposed body forcing (–)
F_z	Axial component of imposed body forcing (–)
K	Nondimensional turbulent kinetic energy (–)
L_{rd}	Dampening radial extent (–)
L_{rt}	Perturbation forcing radial extent (–)
L_{zt}	Perturbation forcing axial extent (–)
P	Nondimensional pressure (–)

R	Nondimensional radial coordinate (–)
R_{0d}	Dampening radial limit (–)
R_{0t}	Perturbation forcing radial origin (–)
R_1	Nondimensional disk outer radius (–)
R_2	Nondimensional disk inner radius (–)
R_d	Dampening helper function (–)
Re	Reynolds number (–)
Re(...)	Real part of ... (–)
Re^*	Local Reynolds number (–)
Re_τ	Wall friction Reynolds number (–)
R_{ij}	Nondimensional velocity two point correlation (–)
T	Nondimensional time (–)
Ta	Taylor number (–)
Ta^*	Local Taylor number (–)
$\mathcal{T}_w$	Nondimensional wall shear stress (–)
$\boldsymbol{U}$	Nondimensional velocity vector (–)
U	Nondimensional velocity magnitude (–)
$\bar{U}_i$	Temporal average of velocity U_i (–)
U_i'	Fluctuating component of velocity U_i (–)
$\boldsymbol{U}_{ic}$	Parabolic analytical velocity field (–)
$\bar{U}_\phi$	Temporal average of circumferential velocity (–)
U_ϕ	Nondimensional circumferential velocity (–)
$\bar{U}_r$	Temporal average of radial velocity (–)
$\mathcal{U}_r'$	Fourier transform of fluctuating component of radial velocity (–)
U_r'	Fluctuating component of radial velocity (–)
U_r	Nondimensional radial velocity (–)
U_τ	Nondimensional friction velocity (–)
U_z	Nondimensional axial velocity (–)
$\mathcal{V}'$	Fourier transform of any nondimensional flow field variable fluctuating component (–)
$\boldsymbol{X}_0$	Two point correlation origin point (–)
X_k	Local coordinate in k-direction, originating from $\boldsymbol{X}_0$ (–)
X_{kmin}	Lower bound of X_k (–)
X_{kmax}	Upper bound of X_k (–)
Z	Nondimensional axial coordinate (–)
Z_{0t}	Perturbation forcing axial origin (–)
Z^+	Nondimensional wall friction coordinate (–)

Lowercase

a	Perturbation interval index (–)
b	Summation series index (–)
b_{max}	Maximum radial perturbation wavenumber index (–)
b_{min}	Minimum radial perturbation wavenumber index (–)
c	Summation series index (–)
c_{max}	Maximum circumferential perturbation wavenumber index (–)
c_{min}	Minimum circumferential perturbation wavenumber index (–)
d	Summation series index (–)
e	Summation series index (–)
$\boldsymbol{e}_z$	Unit vector in axial direction (–)
g_0	Perturbation helper function (–)
g_1	Perturbation helper function (–)
g_2	Perturbation helper function (–)
h_a	Superposition of perturbation modes (–)
i	Imaginary unit (–)
i	Placeholder for arbitrary coordinate direction (–)
j	Placeholder for arbitrary coordinate direction (–)
k	Placeholder for arbitrary coordinate direction (–)
l	Placeholder for arbitrary coordinate direction (–)
$\dot{m}$	Mass flow per disk gap (kg/s)
m	Number of summation series terms (–)
n	Number of summation series terms (–)
n	Total number of spectral elements (–)
n_ϕ	Number of spectral elements in ϕ-direction (–)
n_r	Number of spectral elements in r-direction (–)
n_z	Number of spectral elements in z-direction (–)
p	Pressure (Pa)
p_1	Rotor inlet pressure (Pa)
q	Dampening helper function (–)
r	Radial coordinate (m)
r_1	Outer disk radius (m)
r_2	Inner disk radius (m)
s	Half the disk spacing (m)
t	Time (s)
$\hat{u}_{\phi 1}$	Average circumferential velocity magnitude at r_1 (m/s)
u_ϕ	Circumferential velocity (m/s)
$\hat{u}_{r1}$	Average radial velocity magnitude at r_1 (m/s)
u_r	Radial velocity (m/s)
u_τ	Friction velocity (m/s)
u_z	Axial velocity (m/s)
$\dot{w}$	Power output per disk gap (W)
z	Axial coordinate (m)
z^+	Wall friction coordinate (m)

Greek

α_1	Inlet flow angle (–)
γ_k	Wavenumber in k-direction (–)
γ_ϕ	Circumferential wavenumber (–)
$\gamma_{\phi 0}$	Circumferential perturbation wavenumber step (–)
γ_r	Radial wavenumber (–)
γ_{r0}	Radial perturbation wavenumber step (–)
γ_t	Temporal wavenumber (–)
γ_z	Axial wavenumber (–)
δ_v	Wall friction length scale (m)
Δ_v	Nondimensional wall friction length scale (–)
ϵ	Nondimensional turbulent dissipation (–)
θ	Domain size in circumferential direction (–)
κ_k	Wavenumber in k-direction (–)
λ_d	Dampening strength parameter (–)
λ_t	Perturbation strength parameter (–)
μ	Fluid dynamic viscosity (Pa s)
ν	Fluid kinematic viscosity (m^2/s)
ξ_{abc}	Random perturbation phase shift (–)
ρ	Fluid density (kg/m^3)
σ^*	Local disk gap aspect ratio (–)
σ	Disk gap aspect ratio (–)
τ_w	Wall shear stress (N/m^2)
ϕ	Circumferential coordinate (-)
ω	Angular velocity (1/s)

Appendix B. Abbreviations

CFD	Computational fluid dynamics
DNS	Direct numerical simulation
PTV	Particle tracking velocimetry
RANS	Reynolds averaged Navier–Stokes
SST	Shear stress transport

References

[1] M.C. Breiter, K. Pohlhausen, Laminar Flow Between Two Parallel Rotating Disks, Report No. ARL 62-318, Aeronautical Research Laboratories, Wright-Patterson AFB, Ohio, 1962.

[2] E.W. Beans, Performance Characteristics of a Friction Disc Turbine (Ph.D. thesis), Pennsylvania State University, 1961.

[3] M. Batista, Steady flow of incompressible fluid between two co-rotating disks, Appl. Math. Model. 35 (2011) 5225–5233.

[4] J.E. Flaherty, R.C. DiPrima, Effect of a Coriolis force on the stability of plane poiseuille flow, Phys. Fluids 21 (5) (1978) 718–726, http://dx.doi.org/10.1063/1.862289.

[5] S. Klingl, S. Lecheler, M. Pfitzner, Absolute and convective stability of flow between closely spaced co-rotating disks with imposed throughflow, Eur. J. Mech. B/Fluids 91 (2022) 226–232, http://dx.doi.org/10.1016/j.euromechflu.2021.10.012.

[6] L.L. Pater, E. Crowther, W. Rice, Flow regime definition for flow between corotating disks, J. Fluids Eng. 96 (1) (1974) 29–34, http://dx.doi.org/10.1115/1.3447090.

[7] G. Dibelius, D. Nendl, Reibungsturbomaschinen. Forschungsberichte des Landes Nordrhein-Westfalen, VS Verlag für Sozialwissenschaften, Wiesbaden, 1973, http://dx.doi.org/10.1007/978-3-322-88329-2_1.

[8] E. Appelquist, P. Schlatter, P.H. Alfredsson, R.J. Lingwood, Transition to turbulence in the rotating-disk boundary-layer flow with stationary vortices, J. Fluid Mech. 836 (2018) 43–71, http://dx.doi.org/10.1017/jfm.2017.771.

[9] M. Turkyilmazoglu, Primary instability mechanisms on the magnetohydrodynamic boundary layer flow over a rotating disk subject to a uniform radial flow, Phys. Fluids 21 (7) (2009) 074103, http://dx.doi.org/10.1063/1.3177353.

[10] E. Appelquist, P. Schlatter, P. Alfredsson, R. Lingwood, Turbulence in the rotating-disk boundary layer investigated through direct numerical simulations, Eur. J. Mech. B/Fluids 70 (2018) 6–18, http://dx.doi.org/10.1016/j.euromechflu.2018.01.008.

[11] C. Schosser, Experimental and Numerical Investigations and Optimisation of Tesla-Radial Turbines (Dissertation), Universität der Bundeswehr, München, 2016.

[12] S. Klingl, S. Lecheler, M. Pfitzner, Linear stability investigations on the inward flow between closely spaced co-rotating disks, Eur. J. Mech. B/Fluids 84 (2020) 455–469, http://dx.doi.org/10.1016/j.euromechflu.2020.07.007.

[13] L.L. Pater, Transition of Inward Flow Between Closely Spaced Corotating Disks (Ph.D. thesis), Arizona State University, 1973.

[14] R. Wollkind, R.C. DiPrima, Effect of a coriolis force on the stability of plane poiseuille flow, Phys. Fluids 16 (12) (1973) 2045–2051, http://dx.doi.org/10.1063/1.1694263.

[15] Nek5000, Version 19.0, Argonne National Laboratory, Illinois, 2019, URL: https://nek5000.mcs.anl.gov.

[16] S.G. Klingl, Design Guidelines for Tesla Turbines Based on Comprehensive Theoretical, Numerical and Experimental Investigations (unpublished dissertation, publication expected in 2024), Universität der Bundeswehr, München, 2024.

[17] S.B. Pope, Turbulent Flows, seventh printing ed., Cambridge Univ. Press, Cambridge, 2010.

[18] P. Schlatter, R. Örlü, Turbulent boundary layers at moderate Reynolds numbers: inflow length and tripping effects, J. Fluid Mech. 710 (2012) 5–34, http://dx.doi.org/10.1017/jfm.2012.324.

[19] M. Chevalier, P. Schlatter, A. Lundbladh, D.S. Henningson, SIMSON : A Pseudo-Spectral Solver for Incompressible Boundary Layer Flows, Technical Report 2007:07, KTH, Mechanics, 2007, QC 20120306.

[20] H. Childs, E. Brugger, B. Whitlock, J. Meredith, S. Ahern, D. Pugmire, K. Biagas, M. Miller, C. Harrison, G.H. Weber, H. Krishnan, T. Fogal, A. Sanderson, C. Garth, E.W. Bethel, D. Camp, O. Rübel, M. Durant, J.M. Favre, P. Navrátil, VisIt: An end-user tool for visualizing and analyzing very large data, in: High Performance Visualization–Enabling Extreme-Scale Scientific Insight, 2012, pp. 357–372.

[21] Wolfram Research, Inc., Mathematica 13, 2021, URL: https://www.wolfram.com.

[22] ANSYS Inc., ANSYS CFX, release 19.0, 2018.

[23] H. Schlichting, K. Gersten, Boundary Layer Theory, Springer Berlin Heidelberg, Berlin, Heidelberg, 2017, http://dx.doi.org/10.1007/978-3-662-52919-5_3.